ACS APPLIED MATERIALS & INTERFACES

www.acsami.org

Research Article

Ascorbic Acid-PEI Carbon Dots with Osteogenic Effects as miR-2861 Carriers to Effectively Enhance Bone Regeneration

Wenhuan Bu, Xiaowei Xu, Zilin Wang, Nianqiang Jin, Lili Liu, Jie Liu, Shoujun Zhu, Kai Zhang, Raz Jelinek, Ding Zhou,* Hongchen Sun,* and Bai Yang

Cite This: *ACS Appl. Mater. Interfaces* 2020, 12, 50287−50302

Read Online

ACCESS | Metrics & More | Article Recommendations

ABSTRACT: Nucleic acid transfer has shown significant potential in the treatment of bone damage because of its long lasting local effect and lower cost. Nonviral vectors, such as nanomaterials, with higher biocompatibility are increasedly applied in the study of bone defect repair. Carbon dots with various reactive groups on the surface not only provide a unique surface to carry therapeutic genes, but also some carbon dots have been reported to promote osteogenic differentiation. The bone regeneration effect of carbon dots *in vivo*, however, is rarely investigated. MiR-2861 has revealed osteogenic differentiation effects. In the current study, we created ascorbic acid-PEI carbon dots (CD), which were able to carry miR-2861, by the microwave-assisted pyrolysis method. Results demonstrated that CD had excellent fluorescence stability leading to good fluorescence imaging *in vitro* and *in vivo*. CD was efficiently internalized into bone marrow stromal cells (BMSCs) through the clathrin-mediated endocytosis pathway and distributed in the mitochondria, endoplasmic reticulum, lysosome, and nucleus. Results from alkaline phosphatase staining, alizarin red staining, and reverse transcription real-time PCR (RT-QPCR) showed that our CD indeed had osteogenic effects *in vitro*. Flow cytometry data indicated that CD could efficiently deliver miR-2861 into BMSCs *in vitro*, and CD carrying miR-2861 (CD@miR) had the strongest osteogenic effects. Analyses of hematology, serum biochemistry, and histology showed that CD and CD@miR did not have cytotoxicity and had higher biocompatibility *in vivo*. Most interestingly, CD and miR-2861 in the CD@miR could act synergistically to promote osteogenic differentiation *in vitro* and new bone regeneration *in vivo* remarkably. Our results clearly indicate that the osteogenic CD delivering osteogenic therapeutic gene, miR-2861, can obtain much stronger bone regeneration ability, suggesting that our CD has great potential in future clinical application.

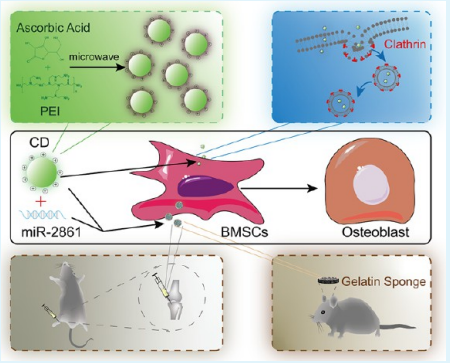

KEYWORDS: *carbon dots, miR-2861, bone marrow stromal cells, bone regeneration, biocompatibility*

INTRODUCTION

Bone damage is a challenging problem in clinical practice.[1] Osteoblasts and their precursors, such as BMSCs, are critical cells involved in bone regeneration. Delivery of therapeutic nucleic acid into BMSCs is a promising method to promote their osteogenic differentiation and mineralization for bone regeneration.[2] MicroRNA (miRNA) is a type of small noncoding RNA that functions as a suppressor of gene expression at the post-transcriptional level and plays a vital role in cell fate determination and differentiation.[3] By virtue of the highly conserved property of miRNA across all animal species, which highlights their evolutionary significance in biological activity, miRNA therapy using miRNA mimics has aroused extensive attention.[4] Compared with traditional plasmid-based gene therapy, small-molecular-weight miRNA mimics make high transfection efficiency more accessible.[4] In addition, miRNA mimics regulate cell function in the cytoplasm for a short term with no need for entry to the nucleus, avoiding the potential genotoxicity caused by continuous and uncontrolled gene expression.[5] It is known that miR-20a, miR-29b, miR-26a, miR-138, and miR-2861 are involved in osteogenic differentiation.[6−10] Interestingly, miR-2861 can target amino acid coding sequences of histone deacetylase 5 (HDAC5) that is involved in degradation of osteogenic transcriptional factor RUNX2, resulting in promoting bone formation. On the other hand, RUNX2 binds to the promoter of the miR-3960/miR-2861 cluster, leading to the induction of miR-3960/miR-2861 transcription.[11] This RUNX2/miR-3960/miR-2861 positive feedback loop can further augment the effect of miR-2861 on osteogenic differentiation.

Received: August 27, 2020
Accepted: October 20, 2020
Published: October 29, 2020

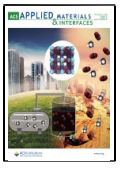

https://dx.doi.org/10.1021/acsami.0c15425
ACS Appl. Mater. Interfaces 2020, 12, 50287−50302

In general, viral vectors are the most efficient system for nucleic acid delivery. However, they may have risk of tumorigenesis, undesired adverse immune response, and so on.[12] Nonviral vectors do not have or have much less side effects of viral vectors, leading to improved attention in recent years.[13] Several studies have used inorganic materials for miRNA delivery including gold nanoparticles, Fe_3O_4 nanoparticles, and silica-based nanoparticles.[14−16] The interactions between these inorganic carriers and miRNAs, however, are usually weak. Polymers, such as polyethylenimine (PEI), poly(lactide-*co*-glycolide) (PLGA), poly(amidoamine) (PAMAMs) dendrimers, or cell-penetrating peptide (CPP), are another type of nonviral system.[4] PEI, a cationic polymer, is considered as a gold standard of nucleic acid transfection.[13] Positively charged PEI can facilitate the interaction with the negatively charged cell membrane to achieve efficient internalization into cells, as well as promote the escape from the lysosome via the "proton sponge" effect to avoid degradation of nucleic acid.[13,17] However, the cytotoxicity of PEI hinders its biological application, provoking to develop PEI-based miRNA carriers with higher biosafety, such as PEI-PEG copolymer or PEI polymer dots.[18,19]

Carbon dots were accidentally discovered during separation and purification of single-walled carbon nanotubes (SWCNTs) in 2004, which created a new class of fluorescent nanomaterials.[20] Compared with traditional fluorescent semiconductor quantum dots, carbon dots display decreased toxicity, eminent biocompatibility, low cost, and chemical inertness accompanied by similar fluorescence properties.[21] Besides, they also possess smaller size (usually less than 10 nm), good solubility, and excellent resistance to photobleaching and various reactive groups, which afford the possibility to be modified by other chemical groups.[22−26] Therefore, carbon dots become a prominent candidate of nucleic acid/drug carrier.[27] Since 2004, a variety of carbon dots have been synthesized by utilizing various precursors and applied in a broad spectrum of applications, such as light-emitting diodes, photocatalysis, biosensing, and nanomedicine.[28−30] In nanomedicine, carbon dots has been used to treat many kinds of diseases, including Parkinson's disease, cancer, and so on.[31,32] It has been reported that some carbon dots can promote osteogenic differentiation.[33−35] These studies, however, only focused on the effect *in vitro*, and there was an absence of evidence for bone regeneration *in vivo*.

Internalization of the vector into the target cell is the foremost step of nucleic acid delivery.[13] Previous studies have shown that nanomaterials are internalized into cells through endocytosis.[36] Energy-dependent endocytic mechanisms in non-phagocytic cell generally include clathrin-mediated, caveolae-mediated endocytosis, and macropinocytosis.[36] As exogenous substances, nanomaterials usually are transferred to the lysosome for degradation.[37] An ideal vector should be capable of escaping from the lysosome. Introducing PEI with the proton sponge effect into the vector could be a splendid choice.

In this study, our goal was to create osteogenic carbon dots with the capacity of carrying miR-2861 to gain synergistic effects on bone regeneration. We synthesized carbon dots (CDs) with ascorbic acid and PEI using the microwave-assisted pyrolysis method. These CDs showed desirable bioimaging ability *in vitro* and *in vivo*. They were internalized into BMSCs by the clathrin-mediated endocytosis pathway and then could locate in the mitochondria, endoplasmic reticulum, lysosome, and nucleus. This CD alone could promote osteogenic differentiation of BMSCs. Most importantly, as a vector, our CD with ameliorative biocompatibility and increased transfection efficiency compared to PEI could facilitate bone regeneration synergistically with miR-2861.

RESULTS AND DISCUSSION

Characteristics of CDs. In our study, we created the CD with ascorbic acid (AA) and PEI (Figure 1A) by the microwave-assisted pyrolysis that endowed the CD with

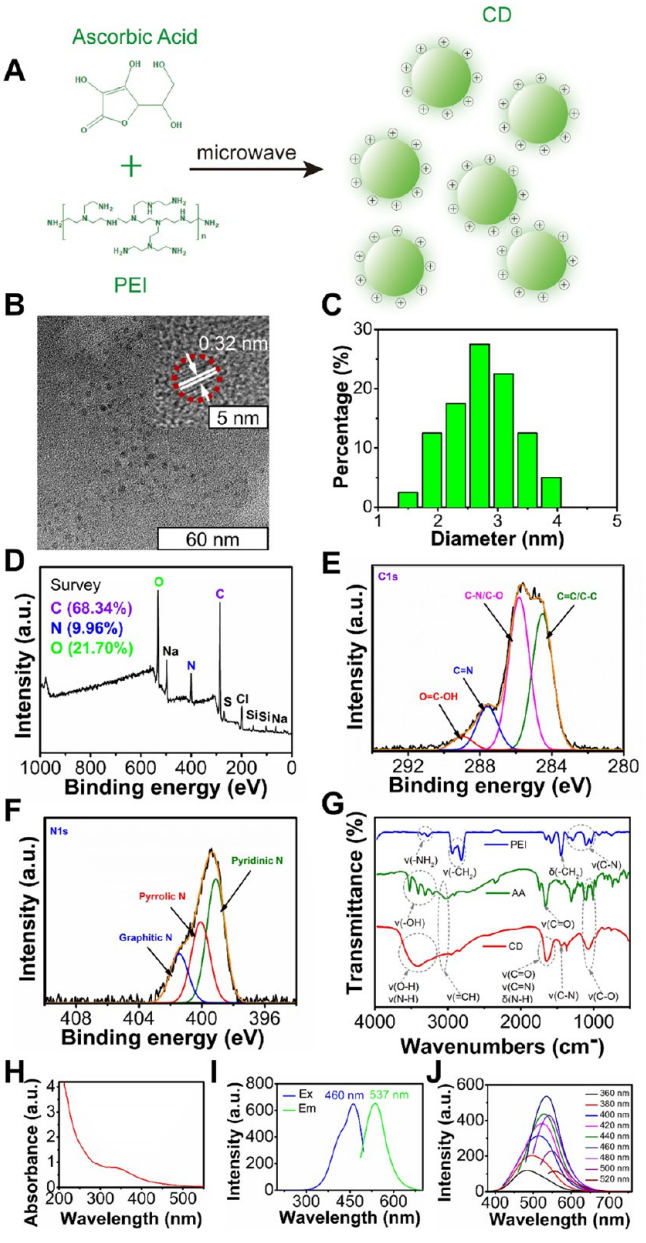

Figure 1. Characteristics of CDs. (A) Schematic illustration of CD preparation through the microwave-assisted pyrolysis method. (B) TEM image and HRTEM image. (C) Size distribution of the CD. (D) XPS analysis of the CD. (E) C1s XPS of the CD. (F) N1s XPS of the CD. (G) FTIR spectra of PEI (blue), AA (green), and CD (red). (H) UV−vis absorption spectrum of the CD. (I) Excitation spectrum (blue) and emission spectrum (green) of the CD. (J) Emission spectrum at excitation wavelength progressively increasing from 360 to 520 nm.

https://dx.doi.org/10.1021/acsami.0c15425
ACS Appl. Mater. Interfaces 2020, 12, 50287−50302

positive charge. The CDs are uniformly dispersed nanoparticles with a size of ~2.5 nm as measured by transmission electron microscopy (TEM) (Figure 1B,C). We also determined the particle size and zeta potential by DLS, which showed 9 nm average hydrodynamic diameter and 33 ± 0.8 mV, respectively. The high-resolution TEM (HRTEM) image showed that the CD had a good crystallization nature with a lattice spacing (~0.32 nm) (Figure 1B), which is a close match with the (002) lattice spacing of graphite. XPS analysis indicated that the CD created herein had three major elements, namely, C, N, and O, on its surface (Figure 1D). The deconvolution of the C1s spectrum displayed four peaks, namely, the O=C−OH peak at 288.5 eV, C=N peak at 287.5 eV, C−N/C−O peak at 285.7 eV, and C=C/C−C peak at 284.5 eV (Figure 1E). The deconvolution of the N1s spectrum displayed pyridinic N (399.2 eV), pyrrolic N (400.1 eV), and graphitic N (401.5 eV) (Figure 1F). Fourier transform infrared (FTIR) was used to further analyze the structure of the CD (Figure 1G). The FTIR spectrum of the CD exhibited =CH stretching vibration at 3033 cm^{-1} and C−O stretching vibration at 1085 cm^{-1}, which came from =CH and C−O of the aromatic ring in the AA. The center of the broad peak at 3450 cm^{-1} was attributed to the stretching vibrations of O−H and N−H, which originated from the hydroxyl of the AA and amidogen of PEI. Compared with the FTIR spectrum of the AA, the increase of relative intensity of 1670 cm^{-1} originating from the C=O group indicated the oxygenation process of CD.[38]

Analyses by UV−vis absorption and fluorescence spectra revealed that our CD had a remarkable optical property. The UV−vis spectrum indicated a shoulder absorption peak at 344 nm for the CD corresponding to the n−π^* transitions (Figure 1H). The radiative relaxation of the n−π^* excitation results in fluorescence.[39] The narrow and symmetrical fluorescence spectrum showed that the emission peak of the CD was at 537 nm at an excitation wavelength of 460 nm (Figure 1I). The full width at half-maximum of the CD was ~65 nm, suggesting a narrow size distribution or limited emissive sites on the surface.[40,41] Furthermore, excitation-dependent fluorescence behavior was observed, similar to most of the fluorescent carbon dots.[21] The emission peak was red-shifted from 483 to 557 nm with excitation wavelength from 360 to 520 nm (Figure 1J), which may be attributed to the optical selection of differently sized nanoparticles (quantum effect) and different emissive trap on the surface of the CD.[42]

Fluorescent Images and Cytotoxicity of the CD. It has been proven that carbon dots have excellent fluorescence stability, which can be used in bioimaging. Therefore, we evaluated if our CD had the same ability *in vitro* and *in vivo*. First, confocal laser scanning microscope (CLSM) images displayed that the CD could be efficiently internalized into BMSCs after 24 h of incubation. As discussed previously, the emission of the CD is excitation-dependent. We observed that the cytoplasm of BMSCs displayed a blue, green, or red color with ultraviolet, blue, and green light excitation *in vitro*, respectively, with optimal fluorescence imaging at blue light excitation, consistent with the result of fluorescence spectra (Figure 2A). Except for BMSCs, other cell lines including preosteoblast MC3T3-E1, keratinocyte HaCaT, and squamous cell carcinoma cell CAL 27 were also used for cell imaging. All of these cells exhibited excitation-dependent fluorescence imaging after incubating with the CD. The strongest imaging

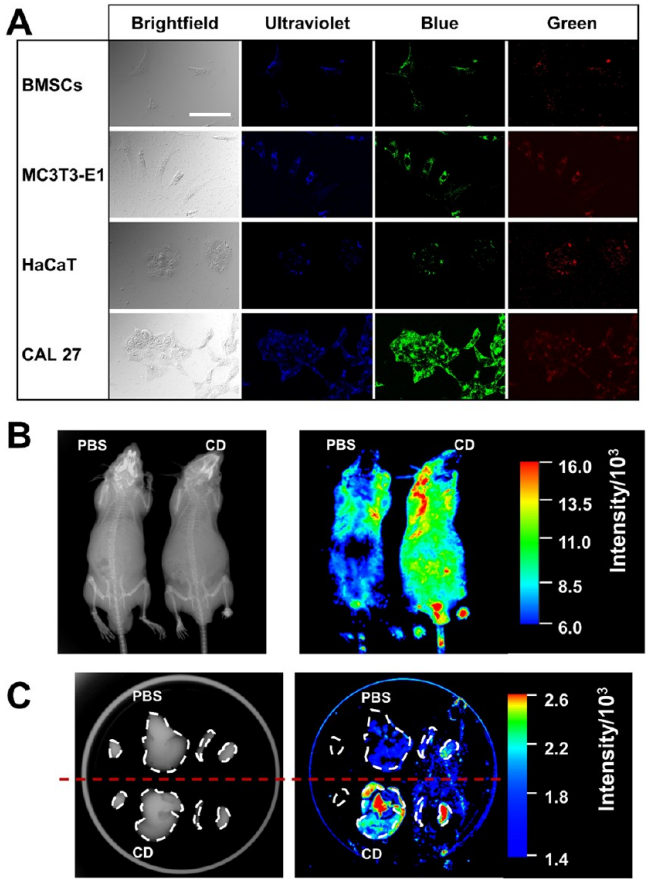

Figure 2. Fluorescence images from cells or mouse tissues treated with CDs *in vitro* and *in vivo*. (A) CLSM images of BMSCs, MC3TC-E1, HaCaT, and CAL 27 treated with CDs at $\lambda_{ex}/\lambda_{em}$ of 359/461, 488/513, and 590/618, respectively. Scale bar, 80 μm. (B) Fluorescence imaging of the nude mouse treated with CDs *in vivo*. It shows that one is a PBS control mouse and another one is a mouse treated with CDs. The image on the left panel is taken under X-rays, and the image on the right panel is under visible light at 390/535 nm wavelength of excitation/emission. (C) Fluorescence images from heart, live, spleen, and kidney, which were collected from mice in panel (B). The top panel is from the mouse treated with PBS. The bottom panel is from the mouse treated with CDs. The image on the left panel is taken under X-rays, and the image on the right panel is under visible light at 390/535 nm wavelength of excitation/emission.

was observed in CAL27, which could be attributed to overactive endocytic activity in cancer cells.[43]

Further, *in vivo* experiments were performed and demonstrated that the CD exhibited obvious fluorescence emission using an *in vivo* imaging system (IVIS) after CDs were injected intravenously into the nude mouse (Figure 2B). To learn the *in vivo* distribution of CDs in detail, organs were removed from the body and imaged. Figure 2C shows that prominent fluorescence signals were observed in liver and kidney. Biodistribution of nanoparticles is associated with a myriad of factors, such as administration route, property of nanoparticles, and physiological environment.[44] It is reported that particles less than 8 nm in diameter may be filtered by the glomerular capillary membrane of kidney into renal tubules and cleared through urine.[45] The positive fluorescence signal in kidney indicates that our CD can be directly excreted in urine. On the other hand, surface charge also influences biodistribution of nanoparticles. It is reported that positively charged

https://dx.doi.org/10.1021/acsami.0c15425
ACS Appl. Mater. Interfaces 2020, 12, 50287−50302

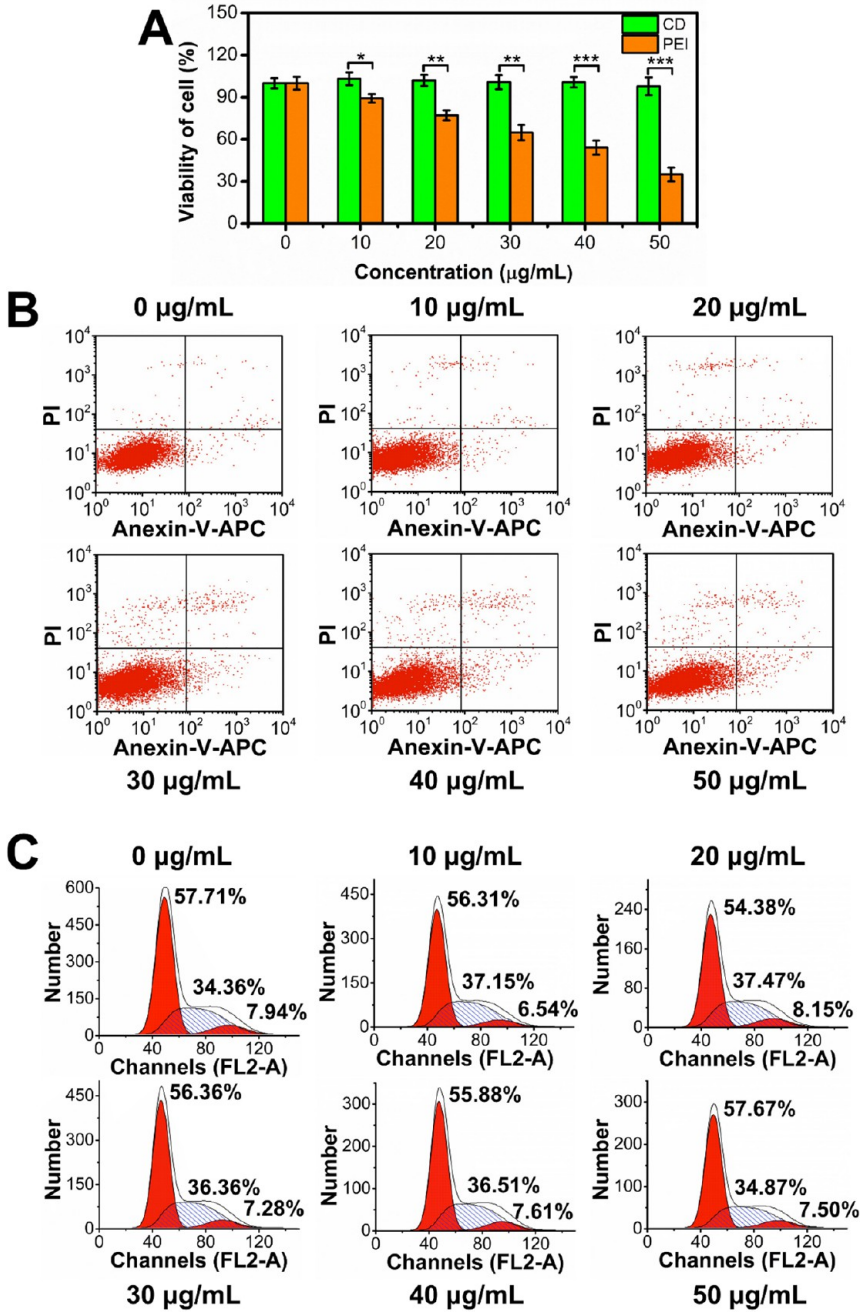

Figure 3. Cytotoxicity assays of CDs using BMSCs *in vitro*. (A) MTT assay of the CD and PEI. (B) Apoptosis analysis. (C) Cell cycle analysis. Data are presented as means ± SD from three experiments.

iron oxide nanoparticles aggregated in liver while negatively charged iron oxide nanoparticles were found in the lymph nodes.[46] Aggregation of our CD in liver can be attributed to the positive charge of the CD, which suggests that our CD can be metabolized via bile.[47]

Whether or not the CD really can be used in the future clinical practice, one major factor is its cytotoxicity. The MTT assay was performed to explore the cytotoxicity of the CD and PEI. The result showed that viability of BMSCs had no significant difference with the dose increase of the CD from 0 to 50 μg/mL, 97.84% at 50 μg/mL (Figure 3A). PEI, however, started to show an inhibition effect even at 10 μg/mL. With the increase of PEI concentration, the viability of BMSCs reduced remarkably, only 35.00% at 50 μg/mL (Figure 3A). As the gold standard of miRNA transfection, PEI's biological application is impeded by its cytotoxicity.[13] In this study, our CD composed of PEI and ascorbic acid showed much more biocompatibility than PEI, which is in favor of biological application. To further determine the biocompatibility of the CD, we performed cell apoptosis and cell cycle assays. Cell apoptosis (Figure 3B) and cell cycle (Figure 3C) assays also revealed no significant difference among different groups. These results indicate that the CD has no cytotoxicity effect for BMSCs and a good biocompatibility *in vitro*.

Cellular Uptake and Intracellular Distribution of CDs. From the previous section, we learn that our CD can be efficiently internalized into cells. To further understand the process of cellular uptake and intracellular distribution of CDs,

https://dx.doi.org/10.1021/acsami.0c15425
ACS Appl. Mater. Interfaces 2020, 12, 50287−50302

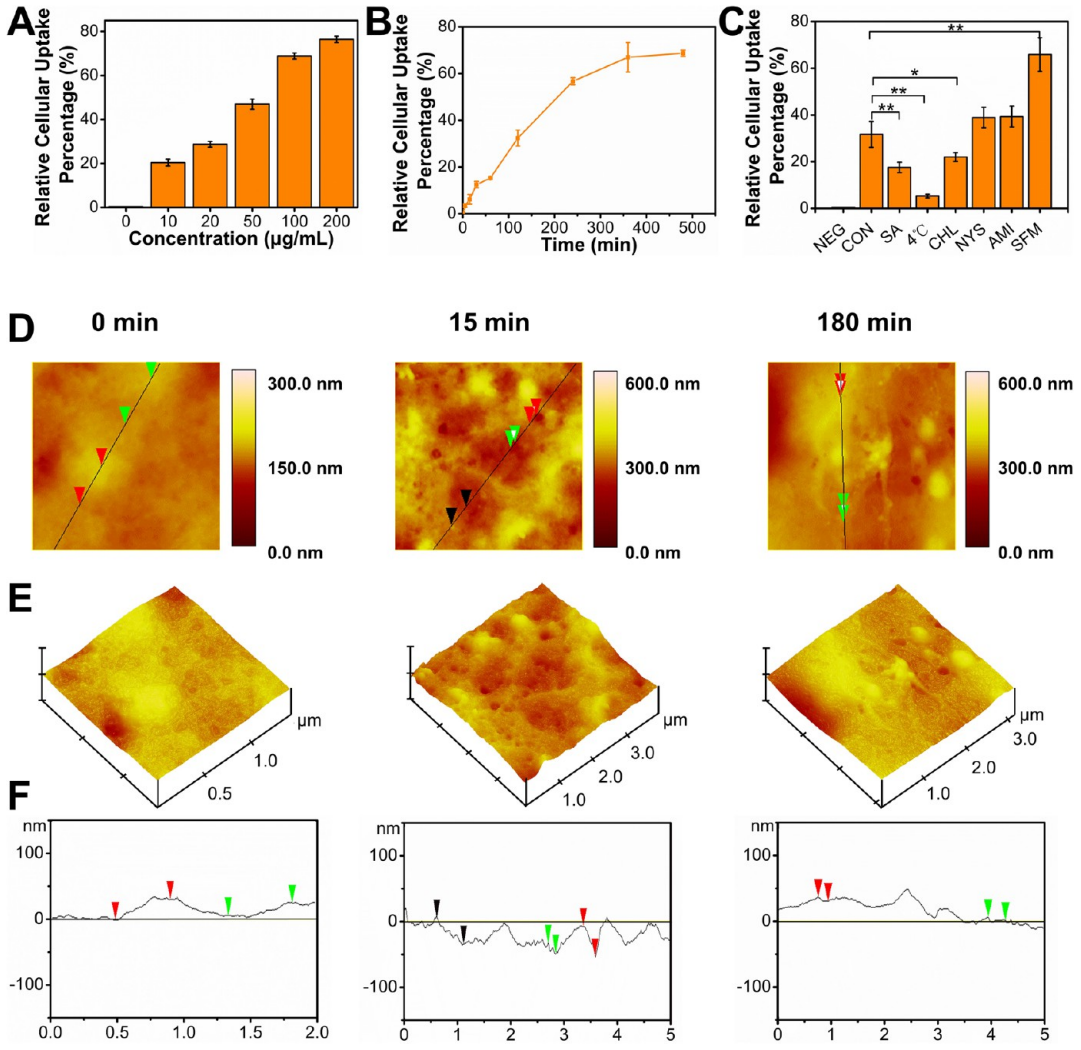

Figure 4. Cellular uptake of CDs. Dose response (A) and time course (B) assays by flow cytometry. (C) Quantitative analysis of the influence factors of uptake. (D) Morphological changes of the BMSC surface after incubating with CDs by AFM scanning (tapping mode) at 0 (left panel), 15 (middle panel), and 180 min (right panel). (E) Enlarged image from the corresponding image in panel (D). (F) Measurements of diameter and depth of the invagination structure for each time point. Data are presented as means ± SD from three experiments. * $P < 0.05$, ** $P < 0.01$, *** $P < 0.001$.

assays of time course and dose response were performed. CD-treated cells were analyzed by flow cytometry, atomic force microscopy (AFM), fluorescence microscopy, and TEM. Flow cytometry data of the dose response showed that cellular uptake elevated with CD dose increasing from 10 to 200 μg/mL after 4 h of incubation (Figure 4A). Next, 100 μg/mL CD dose was used to carry out the time course assay from 5 min to 8 h. Figure 4B reveals that cellular uptake had started before 5 min and exponentially boosted with increasing time before 4 h and then became slow and plateau phases/saturation. This fast internalization may be attributed to electrostatic interaction between the positively charged CD and negatively charged cell membrane, as well as ultrasmall size of the CD.[13] These results indicate that the cellular uptake of the CD is dose-dependent and time-dependent.

To uncover internalization mechanisms of the CD, we used three endocytosis inhibitors, namely, chlorpromazine (CHL, inhibitor of clathrin-mediated endocytosis), nystatin (NYS, inhibitor of caveolin-mediated endocytosis), and amiloride (AMI, inhibitor of macropinocytosis), and energy blockage, namely, sodium azide (SA) and 4 °C treatment, to figure out the main pathway implicated in CD internalization *in vitro*.[48,49] Data from flow cytometry analysis demonstrated (Figure 4C) that cellular uptake of the CD was significantly decreased by CHL treatment (~30% decrease) while the other two kinds of inhibitors could not block CD internalization, suggesting that clathrin-mediated endocytosis is one of the factors that is involved in internalization of CDs. Interestingly, the CD internalization was remarkably reduced by SA (~45% decrease) or lower temperature 4 °C treatment (~83% decrease), especially lower temperature (Figure 4C). It is known that low temperature also decreases the plasma membrane fluidity, leading to lower substance exchange of cells, which may result in more conspicuous inhibition of CD internalization by 4 °C treatment than that by SA treatment.[50,51] It is worth noting that a small part of CDs still could be internalized in SA or 4 °C treatment groups, suggesting that an energy-independent pathway is also involved in CD internalization. We also found that the serum-free medium (SFM) increased cellular uptake of CDs (Figure 4C), which indicates that proteins in the serum can be absorbed on the

https://dx.doi.org/10.1021/acsami.0c15425
ACS Appl. Mater. Interfaces 2020, 12, 50287−50302

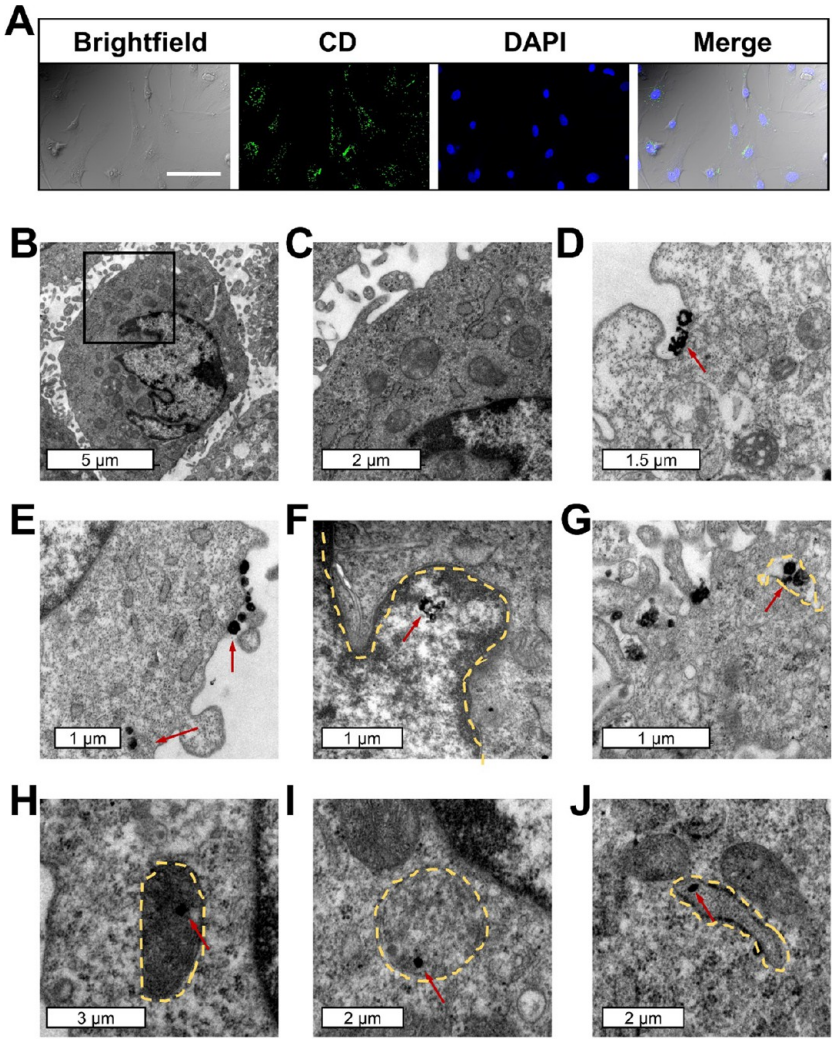

Figure 5. Intracellular distribution of CDs. (A) CLSM images of BMSCs treated with the CD and DAPI. From left to right, BMSCs imaged under bright-field, 488 nm excitation, 359 excitation, and merged image. (B) TEM image of BMSCs without CD treatment. (C) Enlarged image from a part (black rectangle) of panel (B). (D–J) TEM images of BMSCs treated with CDs. Yellow dots outline the subcellular structure (contours of the nucleus, intracellular vesicle, mitochondria, lysosome, and endoplasmic reticulum are shown in panels (F), (G), (H), (I), and (J), respectively). Red arrows point the CD in the BMSCs.

surface of CDs and cells, hindering the interaction between CDs and cells.[52]

Next, we analyzed morphological changes on the surface of cells during the process of cellular uptake of the CD by AFM. Smooth surfaces were observed on the cell membrane of untreated cells (Figure 4D,E). After stimulation for 15 min by the CD, evident invagination emerged on the cell surface (Figure 4D,E). The invagination exhibited ∼200 nm in diameter and ∼50 nm in depth (Figure 4F), which was consistent with a previous report that the size of a clathrin-coated pit has an upper limit about 200 nm in diameter.[53] After cells were incubated with CDs for 180 min, the invaginated cell surface was recuperated (Figure 4D,F). Considering that cellular uptake is still in progress at 180 min determined from Figure 4B, this further verified our supposition that an energy-independent pathway participated in internalization of CDs. Our results are similar to a previous study that uptake of graphene quantum dots with an average lateral size of 20 nm is both energy-dependent and energy-independent.[54] Taken together, clathrin-mediated endocytosis plays an important role in cellular uptake of CDs while an energy-independent pathway is also involved in the process.

In order to understand the distribution of CDs in the cells, we labeled the cell nucleus with DAPI. Data from CLSM showed that most CDs created herein distributed into the cytoplasm and only a small fraction of CDs were internalized into the nucleus (Figure 5A). Considering that the size of nuclear pores is ∼10 nm, it is comprehensible that our CD (1.5−4 nm) could enter into the nucleus.[55]

To further reveal the exact intracellular distribution of CDs, TEM was used to precisely visualize the location of CDs in the cells. After BMSCs were incubated with CDs for 15 min, large and dense aggregated CDs appeared in the invagination of the cell membrane (Figure 5D) and intracellular vesicle (Figure 5G). This phenomenon suggests that the invagination may be formed by clathrin-mediated endocytosis and the intracellular vesicle could be a clathrin-coated pit. Besides, CDs were also found outside the cell membrane without invagination and in the cytoplasm without vesicle encapsulation at 15 min (Figure 5E), which might be internalized by passive transport. When incubated with BMSCs for 180 min, CDs were found in the

https://dx.doi.org/10.1021/acsami.0c15425
ACS Appl. Mater. Interfaces 2020, 12, 50287−50302

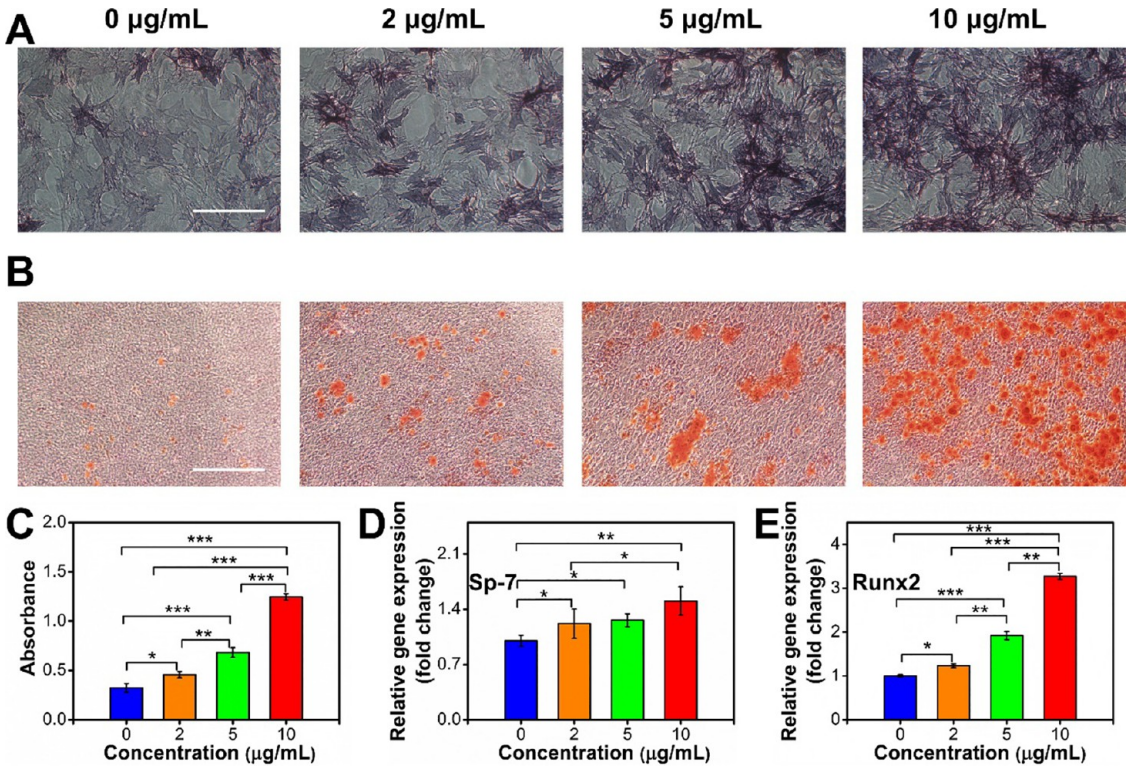

Figure 6. Osteogenic effects of CDs. (A) ALP staining on day 7 post-treatment. Scale bar, 300 μm. (B) ARS on day 21 post-treatment. Scale bar, 300 μm. (C) Relative quantitative data of ARS through calcium nodule elution by 10% cetylpyridinium chloride. (D) SP-7 gene expression on day 3 post-treatment. (E) Runx2 gene expression on day 3 post-treatment. Data are presented as means ± SD from three experiments. * $P < 0.05$, ** $P < 0.01$, *** $P < 0.001$.

nucleus (Figure 5F), mitochondria (Figure 5H), lysosome (Figure 5I), and endoplasmic reticulum (Figure 5J). In our experiments, only a small amount of CDs was found in the lysosome, which suggests that most CDs could escape from the lysosome via the proton sponge effect originating from the positive charge, laying the basis for our CD as a nucleic acid carrier.[17]

Osteogenic Effects of CDs. It has been reported that some carbon dots can promote osteogenic differentiation.[33−35] Furthermore, ascorbic acid, which is the raw material of the CD, can also regulate positively osteogenic differentiation.[56] To verify that if the CD created herein has the same effect on BMSCs, alkaline phosphatase (ALP) staining, alizarin red staining (ARS), and RT-QPCR were performed. ALP is an important marker for osteogenic activity, and ARS is used to identify calcium deposit, which is the crucial action in the late phase of osteoblast differentiation.[57,58] BMSCs were cultured with CDs at 0, 2, 5, and 10 μg/mL for 3 days, 7 days, or 21 days. Data from ALP on day 7 showed that CD-treated BMSCs had more and darker ALP staining than control BMSCs and positive ALP in BMSCs was increased with the increase of CD concentration (Figure 6A). The result from ARS on day 21 demonstrated that CD-treated BMSCs had more calcium deposits than control BMSCs and the extent of ARS also enhanced with the increase of CD concentration (Figure 6B,C). RUNX2 and SP-7 are two vital transcription factors in osteogenic differentiation.[59,60] Data from RT-QPCR on day 3 showed that CDs significantly promoted gene expressions of Runx2 and SP-7 in a dose-dependent manner (Figure 6D,E). It has been reported that SP-7 is the downstream of RUNX2, in which RUNX2 specifically binds to the DNA element in the SP-7 promoter.[61] The increase of Runx2 was more evident than that of SP-7 in this study, which could be attributed to the reason that it needs to take some time to activate transcription of SP-7 by RUNX2. These results clearly indicate that our CD can also facilitate osteogenic differentiation of BMSCs.

Characteristics and Osteogenic Effects of CD@miR. Although our CD alone can promote osteogenic differentiation, a much stronger promotion effect is needed to deal with *in vivo* situations. To elude possible adverse effects of continuous gene expression from the plasmid on cells, we chose miRNA mimics as delivered nucleic acid. A previous study has shown that miR-2861 can promote osteoblast differentiation.[10] Therefore, herein, we used positively charged CDs to carry negatively charged miR-2861 for enhanced effects of osteogenic differentiation. Results from agarose gel electrophoresis revealed completely retarded migration of miR-2861 at a 4:1 weight ratio of the CD and miR-2861, suggesting that miR-2861 fully complexed with the CD at this ratio (Figure 7A). Therefore, this ratio was used to prepare the CD@miR complex in subsequent research. Data from the transfection experiment showed that Cy3-labeled miR-2861 alone cannot be internalized into BMSCs while PEI and CD both can mediate miR-2861 to enter into BMSCs on 24 h post-transfection (Figure 7B). Quantitative analysis by flow cytometry showed 47.44% of transfection efficiency for CD@miR and 17.62% for PEI with miR-2861 (PEI@miR) (Figure 7C). Data of RT-QPCR also confirmed that the miR-2861 level from the CD@miR group was the highest on days 1, 3, and 7 post-transfection and the second was the PEI@miR group (Figure 7D). HDAC5 is the target gene regulated by

https://dx.doi.org/10.1021/acsami.0c15425
ACS Appl. Mater. Interfaces 2020, 12, 50287−50302

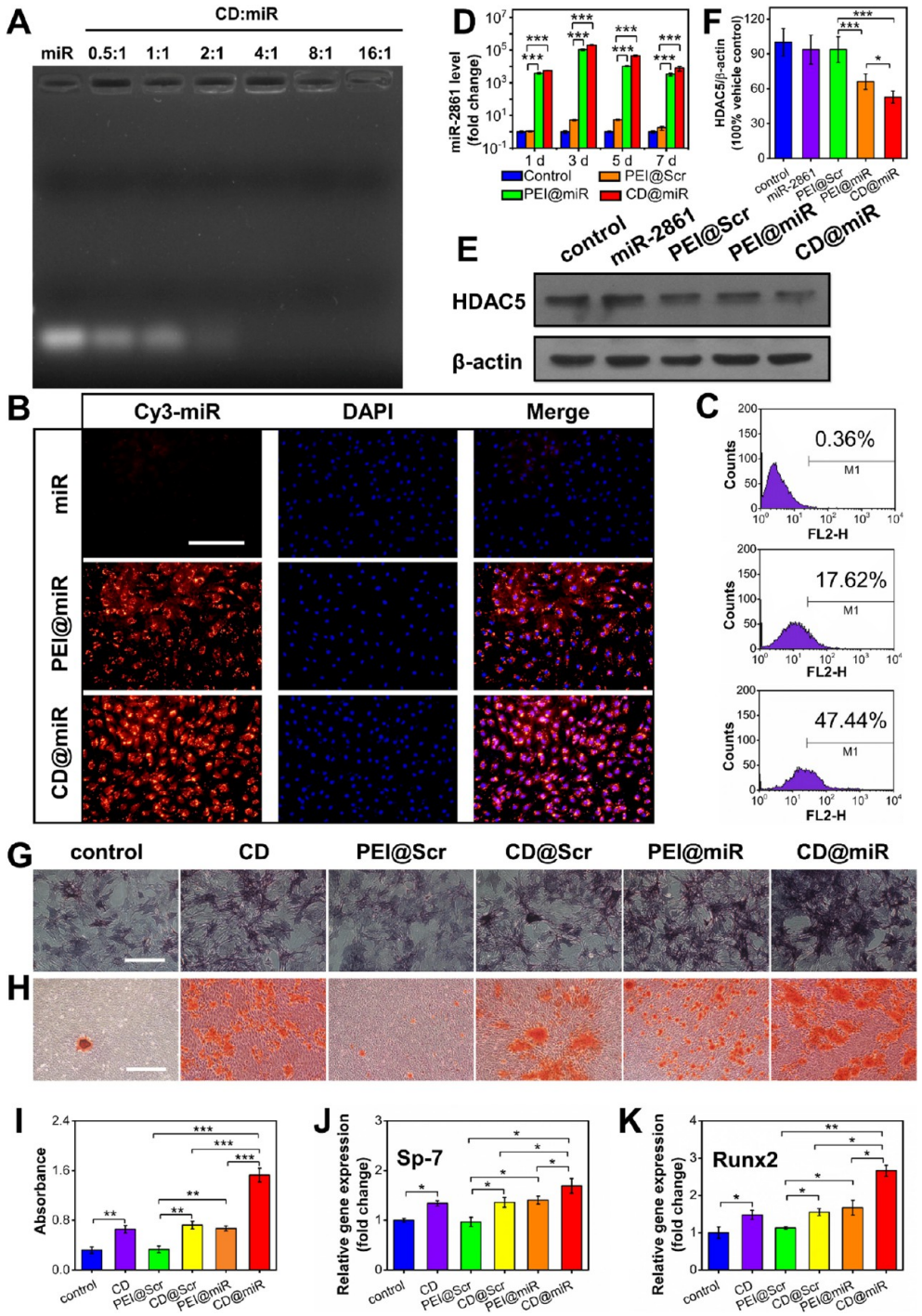

Figure 7. Characteristics and osteogenic effects of CD@miR. (A) Data of agarose gel electrophoresis at various ratios of the CD and miR-2861. (B) Transfection efficiency assay of BMSCs by fluorescence images. miR-2861 was labeled with Cy3. Scale bar, 250 μm. (C) Transfection efficiency by flow cytometry. (D) Levels of miR-2861 in BMSCs on days 1, 3, 5, and 7 post-transfection. (E) Expression of HDAC5 by Western blot on day 2 post-transfection. (F) Quantitative result of Western blot for panel (E). (G) ALP staining on day 7 post-transfection. Scale bar, 300 μm. (H) ARS on day 21 post-transfection. Scale bar, 300 μm. (I) Relative quantitative data of ARS through calcium nodule elution by 10% cetylpyridinium chloride. (J) SP-7 gene expression on day 3 post-transfection. (K) Runx2 gene expression on day 3 post-transfection. Data are presented as means ± SD from three experiments. * $P < 0.05$, ** $P < 0.01$, *** $P < 0.001$.

miR-2861 in osteoblast differentiation.[10] Results from Western blot showed that miR-2861 alone did not affect the HDAC5 protein level while HDAC5 protein expression was significantly decreased after transfection with PEI@miR and CD@miR, especially CD@miR (Figure 7E,F). Currently, there is a consensus that the low transfection efficiency of miRNA remains a bottleneck for miRNA therapy. Although polymers usually have prominent transfection efficiency, their high cytotoxicity limits their further application. Multiple methods have been developed to increase the biocompatibility of polymers such as modification with different functional groups.[62,63] However, these modifications have no effect on

https://dx.doi.org/10.1021/acsami.0c15425
ACS Appl. Mater. Interfaces 2020, 12, 50287−50302

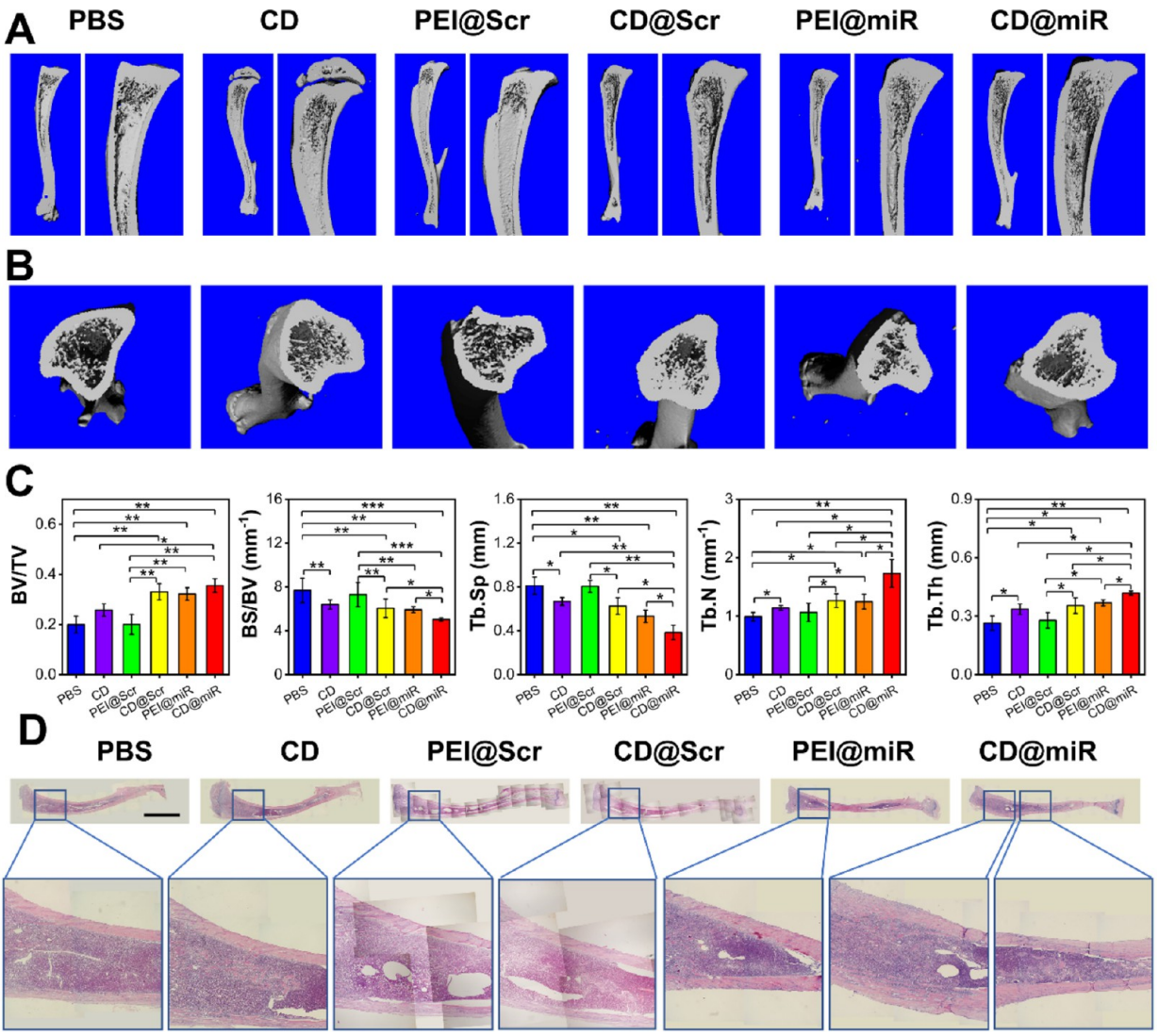

Figure 8. Effects of CD@miR on bone formation *in vivo* in the intra-tibia injection model. (A) Vertical 3D images from right reconstructed tibia by micro CT. (B) Cross 3D images from right reconstructed tibia by micro CT. (C) Trabecular quantitative measurement from right tibia. (D) H&E staining from the same right tibia as panel (A). Scale bar, 0.75 cm. Data are presented as means ± SD. * $P < 0.05$, ** $P < 0.01$, *** $P < 0.001$.

the improvement of transfection efficiency. We used PEI, one of the most commonly used polymers for miRNA delivery, to synthesize CDs with ascorbic acid. Prepared CDs revealed reduced cytotoxicity compared with raw PEI (Figure 3A). Most importantly, enhanced transfection efficiency was observed from CDs, which may benefit from increased cellular uptake of nanometer-sized CDs. These results indicate that CD is an excellent nucleic acid transfer carrier for miR-2861.

Next, we evaluated if our CD could deliver functional miR-2861 to further stimulate osteogenic differentiation. Data from ALP staining showed that ALP activity from the CD@miR group elevated dramatically after 7 days post-transfection compared to other groups (Figure 7G). ARS results also showed that the CD@miR group remarkably had more and larger calcium nodules than the other groups (Figure 7H,I). Consistently, CD@miR significantly increased gene expressions of Runx2 and Sp-7 (Figure 7J,K). It has been reported that miR-2861 indirectly promoted the expression of Runx2 protein through repressing HDAC5 while the mRNA level of Runx2 showed no considerable change by miR-2861.[10] However, in our research, transfection of miR-2861 enhanced the Runx2 mRNA level. Considering that the cell used in our research was distinct from that in the previous study and that miRNAs may have multiple targets even in the same cell, this can be understandable. Indeed, in another research, it is found that the upregulation of miR-2861 was accompanied with increased Runx2 mRNA in human gingival MSCs.[64] In addition to regulation of Runx2 by miR-2861, the Runx2/miR-3960/miR-2861 positive feedback loop played an important role in osteoblast differentiation, in which Runx2 transactivates miR-3960/miR-2861, leading to amplified osteoblast differentiation.[11]

Based on the results above, we believe that the CD is an excellent nucleic acid transfer carrier for miR-2861 and that the CD and miR-2861 in the CD@miR can play synergistic roles in enhancing osteogenic differentiation of BMSCs.

Effects of CD@miR on Bone Regeneration *In Vivo*. Bone regeneration is a well-orchestrated physiological process of bone formation and is also involved in bone defect repair.[2] To evaluate if our CD and its carried miR-2861 can play the synergistic effects on bone regeneration, *in vivo* experiments were required. Therefore, two animal models, intra-tibial

https://dx.doi.org/10.1021/acsami.0c15425
ACS Appl. Mater. Interfaces 2020, 12, 50287−50302

injection for bone formation and calvarial bone defect for bone repair, were used.

In the intra-tibial injection model, data from the vertical section of tibia showed that the CD@miR group had more extended trabeculae into the diaphysis than the other five groups after 1 week post-injection (Figure 8A). Further, quantitative analysis from micro CT revealed that the trabecular bone volume fraction (BV/TV), trabecular number (Tb.N), and trabecular thickness (Tb.Th) increased while trabecular spacing (Tb.Sp) and bone surface density (BS/BV) decreased in the CD@miR group because of new bone formation (Figure 8C). PEI@miR, CD@Scr, and CD alone were second, third, and fourth, respectively (Figure 8C). Data from the cross section also showed that the CD@miR group had the most cortical thickness followed by PEI@miR, CD@Scr, and CD alone. (Figure 8B). H&E staining further confirmed that the CD@miR group had the highest trabecular bone formation, even extended to mid-diaphysis (Figure 8D).

In the calvarial bone defect model, gelatin sponge was used as a scaffold for the CD and miRNA to implant into defect area. Data from micro CT showed that there was scarcely new bone in the PBS and PEI@Scr groups and there were abundant and scattered new bones generated at the edge and center of the defect in the CD and CD@Scr groups on week 12 (Figure 9A,B). Interestingly, CD@miR formed much more new bones

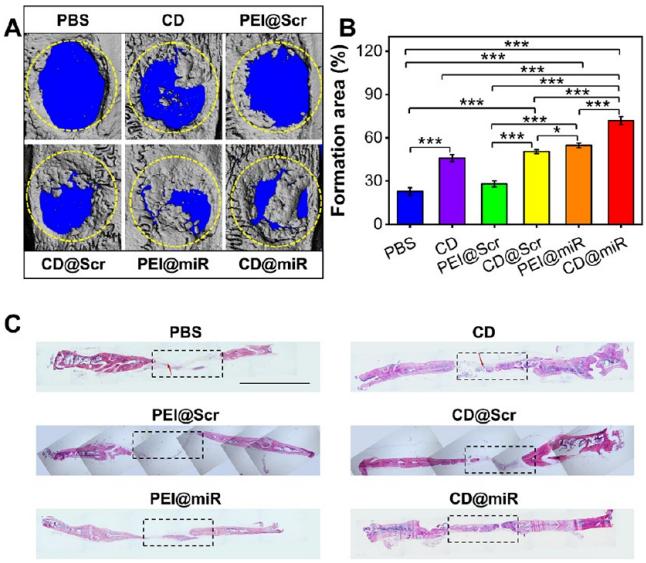

Figure 9. Effects of CD@miR on bone repair *in vivo* in the calvarial bone defect model. (A) 3D image from a reconstructed cranium by micro CT. Yellow dashed circles show the defect area created before treatment. (B) Bar graph of new bone formation for panel (A). (C) H&E staining from the same samples as in panel (A). The black dotted rectangle shows the original defect area. Red arrows point to the the gelatin sponge residue. Scale bar, 0.5 cm. Data are presented as means ± SD. * $P < 0.05$, ** $P < 0.01$, *** $P < 0.001$.

and covered almost 71% of bone defect area although PEI@miR also generated more new bones and covered almost 54% of bone defect area (Figure 9A,B). H&E staining demonstrated that defect areas of the PBS and PEI@Scr groups were mainly filled with connective tissues (Figure 9C). A bony bridge emerged to connect the defect fringe and the mature bone structure could be observed in the CD, CD@Scr, and PEI@miR groups (Figure 9C). Newly formed bone encompassed by the osteoblast, however, almost completely covered the defect area in the CD@miR group (Figure 9C).

Recently, many studies reported miRNA delivery systems for osteoblast differentiation. However, in vivo studies are still few, and the effect of bone regeneration is restricted.[65−67] In these studies, polyurethane nanomicelles, silica nanoparticles, and lipidoids were used only as carriers to assist in transfection of miRNAs. While in our research, in addition to delivering miRNA, CDs exhibited a remarkable ability to promote bone regeneration, revealing the superiority of our miRNA delivery system. Repairing bone defects, especially big bone defects, is still a big challenge for clinicians. Many previous studies show that they have a difficulty to get new bone to cover over 70% of defect area.[68−70] With the synergistic effect of the CD and miR-2861, we can repair bone defects dramatically up to 71%. Taken together, CDs can effectively deliver miR-2861 *in vivo* and promote bone regeneration synergistically. The study herein demonstrates that CD@miR has a potential benefit for bone injury treatment in clinical practice.

Biocompatibility of CD@miR *In Vivo*. Biocompatibility is always a major concern of nanomaterial-based nucleic acid delivery systems for clinical application. Although very little of the gelatin sponge residue could be found in the bone defect area, we did not observe an inflammation response around the residue (Figure 9C). All rats used in this study were alive until the termination of the experiment. Data from hematological analysis including red blood count (RBC), platelet count (PLT), white blood count (WBC), hemoglobin (HGB), hematocrit (HCT), and mean corpuscular hemoglobin (MCH) as well as serum biochemistries including alanine aminotransferase (ALT), aspartate aminotransferase (AST), alkaline phosphatase (ALP), blood urea nitrogen (BUN), creatinine (CREA), and total bilirubin (TBIL) did not show any significant difference in all six groups on day 7 post-treatment (Figure 10A). Histological analysis from H&E staining did not reveal histological abnormity in the heart, liver, spleen, and kidney in all six groups (Figure 10B). Therefore, our results demonstrate that CD@miR has no side effect on hematology and no toxicity for visceral organs, suggesting that CD@miR has excellent biocompatibility for *in vivo* application.

CONCLUSIONS

CDs synthesized in this study not only have excellent fluorescence stability but also the ability to promote osteogenic differentiation and as nucleic acid transfer carriers. Our CD can be internalized into BMSCs by the clathrin-mediated endocytosis pathway and then locates in the mitochondria, endoplasmic reticulum, lysosome, and nucleus. We demonstrated that our CD is able to efficiently deliver miR-2861 into cells without cytotoxicity and with higher biocompatibility *in vitro* and *in vivo*. Importantly, CDs and miR-2861 in CD@miR play synergistical roles in osteogenic differentiation *in vitro* and new bone formation *in vivo* (recovering ~71% of defect bone area) dramatically, which suggests that our CD has stronger potential in future clinical application.

EXPERIMENTAL SECTION

Synthesis of CDs. The CD was synthesized by the microwave-assisted pyrolysis method. Briefly, 0.5 g of ascorbic acid (Sigma-Aldrich, St. Louis, MO, USA) and 0.125 g of PEI 25 K (Sigma-Aldrich) were dissolved in 10 mL of PBS under ultrasonication for 3 min to form a homogeneous solution, microwaved (700 W) for 5 min, then cooled at room temperature for 5 min, and dissolved in 40 mL of

https://dx.doi.org/10.1021/acsami.0c15425
ACS Appl. Mater. Interfaces 2020, 12, 50287−50302

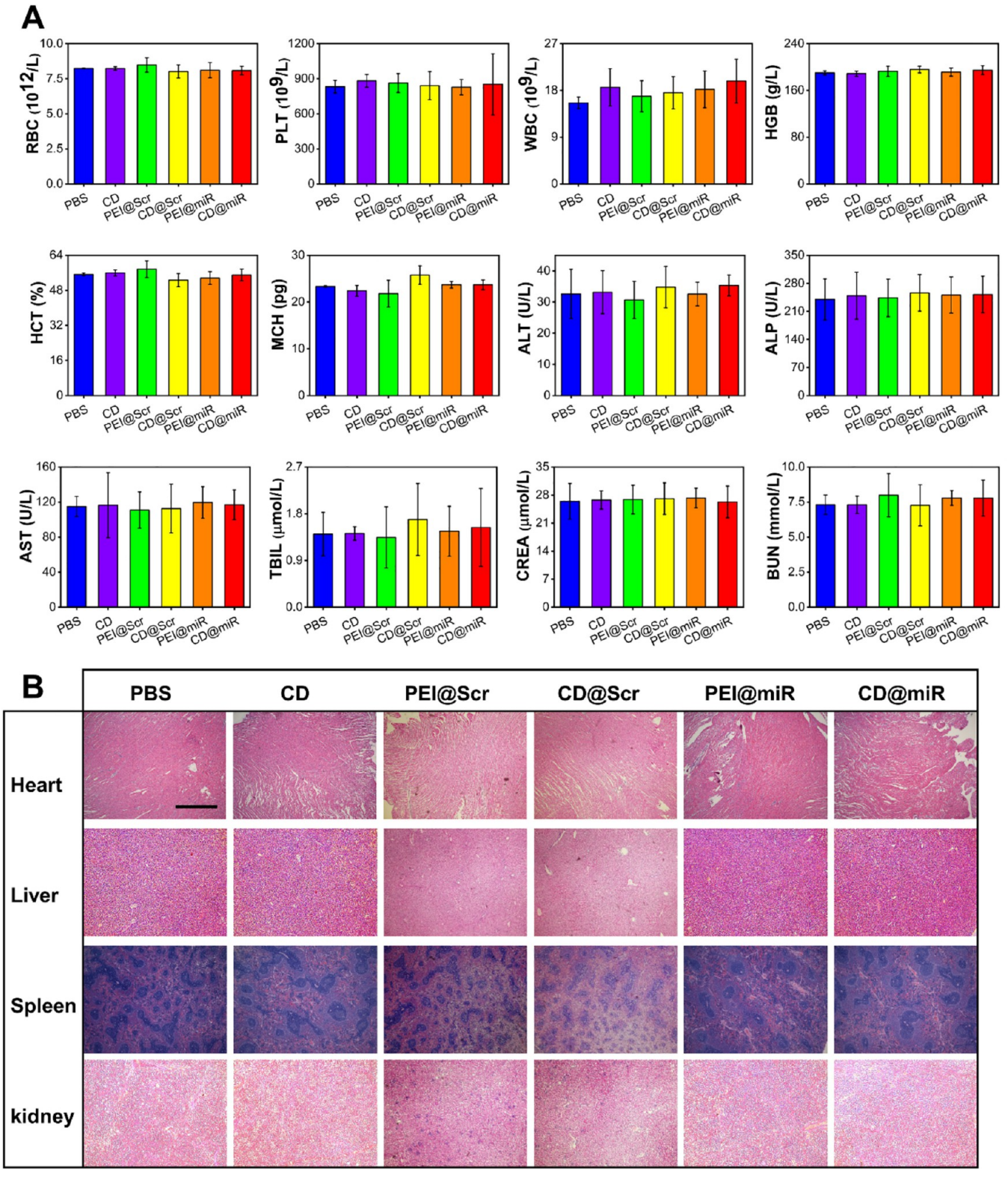

Figure 10. Evaluation of CD biocompatibility and toxicity *in vivo*. (A) Blood samples from the intra-tibia injection model were examined by hematological analysis and serum biochemistries on day 7. All data are presented as means ± SD. No statistical differences were found in all six groups. (B) Histological evaluation of CD toxicity by H&E staining. Heart, liver, spleen, and kidney from the calvarial bone defect model were examined on week 12. Scale bar, 1 mm.

deionized water. This yellow solution was centrifuged at 5200*g* for 5 min and filtered through a 0.22 μm membrane to remove large particles. The supernatant was dialyzed with deionized water in a dialysis bag (MWCO = 3.5 KD) for 7 days. Finally, clear, light yellow CD solution was lyophilized to yield a powdered material.

Characterization of CDs. To determine the detailed physical properties of our CD, TEM (Hitachi H-800 electron microscope at 200 kV acceleration voltage with a CCD camera, Hitachi, Tokyo, Japan) and HRTEM (JEM-2100F electron microscope at 200 kV, JEOL, Tokyo, Japan) were used. Zeta potential was analyzed by

https://dx.doi.org/10.1021/acsami.0c15425
ACS Appl. Mater. Interfaces 2020, 12, 50287−50302

dynamic light scattering (DLS) (Malvern Panalytical, Malvern, UK). A Lambda 800 UV−vis spectrophotometer was used to obtain UV−vis spectra. A Shimadzu RF-5301 PC spectrophotometer (Shimadzu, Kyoto, Japan) was used to acquire fluorescence spectra. FTIR spectra were obtained using a Nicolet AVATAR 360 FTIR instrument (Analytical Instruments, MN, USA). X-ray photoelectron spectroscopy (XPS) was performed using a VG ESCALAB MKII spectrometer with Mg KR excitation (1253.6 eV)(Thermo Fisher Scientific, Waltham, MA, USA).

Cell Culture. BMSCs were isolated from femurs and tibias of 4 week old Wistar rats. The epiphyseal growth plates were removed, and bone marrow was collected by flushing with a DMEM medium (Gibco, Waltham, MA, USA) containing 20% FBS, 100 U/mL penicillin, and 100 mg/mL streptomycin with a 25 gauge needle. Cells were centrifuged at 1500 rpm for 5 min and resuspended with the fresh medium, plated at 1×10^6 cells/flask in a 25 cm^2 culture flask, and incubated at 37 °C in humidified 5% CO_2. The growth medium was changed every 2−3 days. After first trypsinization, cells were cultured with a DMEM medium containing 10% FBS, 100 U/mL penicillin, and 100 mg/mL streptomycin. Cells at passages 3−5 were used for our experiments. For osteogenic induction, 50 μg/mL ascorbic acid and 10 mM β-glycerophosphate were added into the medium. After 3 days, cells were harvested to extract RNA, which were used to check osteogenic gene expressions by RT-QPCR. After 7 days, cells were stained with ALP. ARS was performed on day 21 culture.

MC3T3-E1, HaCaT, and CAL27 were obtained from Nanjing Keygen Biotech Company (China). These cells were grown in a DMEM medium containing 10% FBS with 100 units/mL penicillin and 100 μg/mL streptomycin in a 37 °C humidified incubator containing 5% CO_2.

Fluorescence Images of CD-Treated BMSCs or Mouse *In Vitro* and *In Vivo*. For *in vitro* imaging, BMSCs were plated at 1.5×10^5 cells/well in 6-well plates for 24 h. The growth medium was replaced by a growth medium with 50 μg/mL CDs. After 24 h of incubation, cells were washed with PBS three times, then fixed with 4% paraformaldehyde at 37 °C for 10 min, and washed twice with PBS again. Samples were observed by CLSM.

All animal procedures were performed under the Guideline for Care and Use of Laboratory Animals of Jilin University and approved by the Institutional Animal Care and Use Committee of Jilin University. Six nude mice were divided into two groups: PBS-treated group and CD-treated group. 200 μL of CDs at 2 mg/mL or 200 μL of PBS was injected into the caudal vein. Mice were anesthetized and imaged using a Kodak (Rochester, NY, USA) IVIS with an excitation/emission wavelength at 390/535 nm. Then mice were euthanized, and the heart, liver, spleen, and kidney were harvested for ex vivo imaging under the same parameters.

Cytotoxicity Assays. Cytotoxicity of CDs *in vitro* was evaluated by the MTT assay, apoptosis analysis, and cell cycle assessment. CD solution was filtered through a 0.22 μm membrane to eliminate microbial contamination before incubating with cells. BMSCs were seeded at 8×10^3/well in 96-well plates for 24 h followed by incubating with 200 μL of a growth medium containing CDs at 0, 10, 20, 30, 40, or 50 μg/mL for 24 h. Then, 20 μL of 3-(4,5-dimethyl-2-thiazolyl)-2,5-diphenyl-2*H*-tetrazolium bromide (MTT, 5 mg/mL, Sigma-Aldrich) was added in each well and incubated for 4 h. Finally, the supernatant was removed, and 150 μL/well of dimethyl sulfoxide (DMSO, Sigma-Aldrich) was added. A microplate reader was used to measure the absorbance at 570 nm. Cell viability was calculated through eq 1:

$$\text{cell viability}(\%) = \text{absorbance of the CD-treated group}/\text{absorbance of the control group} \times 100 \quad (1)$$

Apoptosis analysis was performed by the Annexin V-APC Apoptosis Analysis Kit (Tianjin Sungene Biotech, Tianjin, China). Briefly, BMSCs treated with different concentrations of CDs were collected, washed with cold PBS, and then resuspended in 100 μL of binding buffer. 5 μL of Annexin V-APC and 5 μL of PI solution were added in the cell solution for 15 min at room temperature, and then flow cytometry analysis was performed (Becton, Dickinson and Company, Franklin Lakes, NJ, USA).

For cell cycle analysis, BMSCs treated with different concentrations of CDs were collected, fixed with cold ethanol for 1 h at room temperature, washed with cold PBS, then resuspended/incubated in 0.5 mL of PI/RNase staining solution (Tianjin Sungene Biotech) for 30 min at room temperature, and analyzed by flow cytometry.

Cellular Uptake Kinetics. BMSCs were seeded at 1×10^5 cells/well in 6-well plates for 24 h and then incubated with different concentrations (10, 20, 50, 100, 200 μg/mL) of CDs for 4 h for the dose-dependent uptake assay while incubated with 100 μg/mL CDs for different times (5, 15, 30, 60, 120, 240, 360, 480 min) for the time-dependent uptake assay. Cellular uptake was evaluated by flow cytometry.

Cellular Uptake Pathways. BMSCs were seeded at 1×10^5 cells/well in 6-well plates for 24 h. For the energy-dependent uptake assay, cells were precooled at 4 °C or pretreated with 10 mM sodium azide (SA) at 37 °C for 45 min, and then CDs were added/incubated at 100 μg/mL for 1 h. For endocytosis evaluation, uptake pathway inhibitors were used. Cells were pretreated with CHL (10 μg/mL) (Sigma-Aldrich), NYS (50 μg/mL) (Sigma-Aldrich), or AMI (50 μM) (Sigma-Aldrich) for 45 min, and then CDs were added/incubated at 100 μg/mL for 1 h. For the serum-free medium (SFM) group, cells were pretreated with SFM for 45 min, and then CDs in SFM were added/incubated at 100 μg/mL for 1 h. Cellular uptake was evaluated by flow cytometry. Cells only treated with CDs at 100 μg/mL or no treated cells were used for control groups.

AFM was used to evaluate morphological change of the cell surface at different stages of CD uptake. BMSCs were seeded/cultured at 1×10^4 cells a in chamber coverglass for 24 h, then incubated with CDs at 100 μg/mL for 15 or 180 min, washed three times with cold PBS, fixed with freshly prepared 4% cold paraformaldehyde for 20 min, and washed three times with cold PBS. Air-dried cells were scanned in tapping mode AFM with a Nanoscope IIIa scanning probe microscope (Digital Instruments, Bresso, Italy).

Intracellular Distribution of CDs by TEM. BMSCs were seeded at 1×10^5 cells/well in 6-well plates for 24 h. CDs were added at 100 μg/mL and incubated for 15 or 180 min. After washing three times with PBS, cells were trypsinized, harvested, and centrifuged. Cells were fixed with 2% glutaraldehyde in 0.1 M sodium cacodylate buffer at pH 7.4 at room temperature overnight. Then, cells were washed with 0.1 M sodium cacodylate buffer for 10 min three times, further fixed with 1% osmium tetroxide in 0.1 M sodium cacodylate buffer for 1 h, washed with PBS three times, dehydrated in a graded series of ethanol ending with propylene oxide, and embedded in EPON. Then, 70 nm thin sections were prepared with a Reichert Ultracut E ultramicrotome. The sections were observed using a JEM-2100F HRTEM (JEOL, Tokyo, Japan) operating at 120 kV accelerating voltage.

Agarose Gel Electrophoresis. MiR-2861 was dissolved in deionized water to form 1 μg/mL solution. Equal volume of solution containing different concentrations of CDs (0, 0.5, 1, 2, 4, 8, or16 μg/mL) was added to the miR-2861 solution followed by pipetting up and down to make the mixture homogeneous thoroughly. Then the mixture was incubated to form the CD@miR-2861 complex at room temperature for 30 min followed by mixing 8 μL of each solution with 2 μL of loading buffer and loading into 1% agarose gel containing ethidium bromide (0.5 μg/mL) to run at a constant voltage of 100 V for 40 min. The band of miR-2861 was visualized under a UV transilluminator at a wavelength of 365 nm.

Transfection Efficiency *In Vitro*. BMSCs were seeded at 1.0×10^5 cells/well in 6-well plates for 24 h. When cell confluency was ~60%, the growth medium was replaced with the serum-free medium. Freshly prepared complexes of CDs and Cy3-labeled miR-2861 (CD@miR) were added into the well. After 4 h of incubation, the medium with CD@miR was replaced by the growth medium and cultured for 24 h. Transfection efficiency was analyzed by flow cytometry.

https://dx.doi.org/10.1021/acsami.0c15425
ACS Appl. Mater. Interfaces 2020, 12, 50287−50302

Gene Expression by RT-QPCR. BMSCs were seeded at 1×10^5 cells/well in 6-well plates for 24 h. Then, cells were treated differently, cultured for 72 h, and harvested to extract total RNA by the Qiagen RNeasy mini purification kit (Qiagen, Valencia, CA, USA). Reverse transcription reaction was performed with 1 μg of total RNA of each sample using the iScript cDNA synthesis kit (Takara, Tokyo, Japan). RT-QPCRs were performed to determine expression levels of SP-7, Runx2, and β-actin (used as internal control) using the SYBR-Green Preminx Ex Taq (Takara) with a MxPro Mx3005P real-time PCR detection system (Agilent Technologies, Santa Clara, CA, USA). Primers SP-7 F (5′-CATCCATGCAGGCATCTCA-3′)/SP-7 R (5′-CTGCCCACCACCTAACCAA-3′), primers Runx2 F (5′-CATGGCCGGGAATGATGAG-3′)/Runx2 R (5′-TGTGAA-GACCGTTATGGTCAAAGTG-3′), and primers β-actin F (5′-GGAGATTACTGCCCTGGCTCCTA-3′)/β-actin R (5′-GACT-CATCGTACTCCTGCTTGCTG-3′) were used.

Western Blot Assays. BMSCs were seeded at 1×10^5 cells/well in 6-well plates for 24 h. Then, cells were treated differently, cultured for 48 h, harvested, washed with cold PBS three times, and lysed in RIPA containing the protease inhibitor (MedChemExpree, Monmouth Junction, NJ, USA). Lysates were centrifuged at 13,145*g* for 20 min, and supernatants were collected. Proteins in the sample were separated by 8% SDS-PAGE and transferred onto PVDF membranes. Membranes were blocked with 5% BSA in TBST for 2 h, then incubated with the HDAC5 antibody (1:1000, Cell Signaling Technology, Danvers, MA, USA) or β-actin antibody (1:1000, Proteintech, Rosemont, IL, USA) overnight at 4 °C, washed, and incubated with secondary antibodies (1:5000, Proteintech). Signals were detected by an ECL detection reagent using a Tanon 5200 Chemiluminescent Imaging System (Tanon, Shanghai, China). Results were normalized to the internal control β-actin.

Alkaline Phosphatase Staining. BMSCs were seeded at 1×10^5 cells/well in 6-well plates for 24 h. Then, cells were treated differently and cultured in an osteogenic induction medium for 7 days. Cells were stained with the Leukocyte Alkaline Phosphatase Kit (Sigma-Aldrich).

Alizarin Red Staining. BMSCs were seeded at 1×10^5 cells/well in 6-well plates for 24 h. Then, cells were treated differently, cultured in an osteogenic induction medium for 21 days, then fixed with ice-cold 70% ethanol for 1 h, rinsed twice with deionized water, stained with 1% alizarin red S in deionized water (pH 8.3) for 30 min at 37 °C, and washed with deionized water. Calcium nodules were observed under an inverted optical microscope. The stain was eluted through incubating the stained cell with 10% cetylpyridinium chloride for 1 h. The absorbance of the collected dye was read at 540 nm using a microplate reader.

Bone Regeneration *In Vivo*. To evaluate the bone regeneration effect, two animal models were used: one is the intra-tibial injection for bone formation, and the other one is the calvarial bone defect for bone repair. All animal procedures were performed under the Guideline for Care and Use of Laboratory Animals of Jilin University and approved by the Institutional Animal Care and Use Committee of Jilin University. Thirty male Wistar rats (160−200 g) were used for each model and randomly divided into six groups: PBS, CD, PEI@Scr (PEI with scrambled miRNA), CD@Scr (CD with scrambled miRNA), PEI@miR (PEI with miR-2861), and CD@miR (CD with miR-2861) (n = 5).

For the intra-tibial injection model, rats were anesthetized, then injected with 10 μL of PBS, CD (2 mg/mL), PEI@Scr (0.5 mg/mL PEI and 40 μM scrambled miRNA), CD@Scr (2 mg/mL CD and 40 μM scrambled miRNA), PEI@miR (0.5 mg/mL PEI and 40 μM miR-2861), or CD@miR (2 mg/mL CD and 40 μM miR-2861) into the right tibial marrow space. One week after injection, right tibias were excised, fixed in 4% paraformaldehyde solution for 48 h, and then analyzed by micro CT. Bone morphology parameters of the proximal tibial metaphysis and mid-diaphysis were quantified using a Scanco Medical μCT 35 system (Scanco Medical AG, Bassersdorf, Switzerland). These included BV/TV, BS/BV, Tb.Sp, Tb.N, and Tb.Th. A distance of 1.68 mm distal from the growth plate of metaphysis was the start point to evaluate for trabecular bone at 12 μm resolution and 55 keV intensity settings, and from 1.68 to 9.68 mm for cortical bone. Reconstructed solid 3D images were then used to quantify the bone microarchitecture.

For the calvarial bone defect model, rats were anesthetized, and a defect was made in a sagittal plane across the cranium using a 5 mm diameter hollow trephine bur. After removing the trephined calvarial disk, a gelatin sponge loaded with 200 μL of PBS, CD (1.2 mg/mL), PEI@Scr (0.3 mg/mL PEI and 25 μM scrambled miRNA), CD@Scr (1.2 mg/mL CD and 25 μM scrambled miRNA), PEI@miR (0.3 mg/mL PEI and 25 μM miR-2861), or CD@miR (1.2 mg/mL CD and 25 μM miR-2861) was applied to the defect site. Twelve weeks after surgery, cranium bones were excised, fixed in 4% paraformaldehyde solution for 48 h, and then analyzed by micro CT. Specimens were scanned using a Scanco Medical μCT 35 system at a spatial resolution of 15 μm (1 mm aluminum filter, 100 kV, 100 mA) and 500 projections/180°. Reconstructed solid 3D images were then used to quantify the bone microarchitecture.

After micro CT imaging, samples were immersed in 50% formic aid solution for decalcification for 7 days. Then, the samples were dehydrated in a series of ethanol and embedded in paraffin, and 5 μm sections were prepared for hematoxylin and eosin staining (H&E staining).

Biocompatibility Assay *In Vivo*. Blood samples from the intra-tibial injection model were collected for hematology and serum biochemistry analyses. A hematology analyzer (MEK-7222 K; Nihon Kohden, Tokyo, Japan) was used for hematological parameters. Serum biochemistry was analyzed by the ALT, AST, ALP, BUN, CREA, TBIL commercial kit (Roche Diagnostics, Mannheim, Germany). The heart, liver, spleen, and kidney from the calvarial bone defect model were collected for H&E staining.

Statistical Analysis. All experiments *in vitro* were repeated three times. Data were presented as mean ± standard deviation (SD). Statistical analyses were conducted by one-way ANOVA. P value < 0.05 was considered for statistical difference.

AUTHOR INFORMATION

Corresponding Authors

Ding Zhou − *State Key Laboratory of Luminescence and Applications, Changchun Institute of Optics, Fine Mechanics and Physics, Chinese Academy of Sciences, Changchun 130033, China*; Phone: 86-431-86176029; Email: zhouding@ciomp.ac.cn; Fax: 86-431-86176029

Hongchen Sun − *Liaoning Provincial Key Laboratory of Oral Diseases, School of Stomatology and Department of Oral Pathology, School of Stomatology, China Medical University, Shenyang 110001, China*; orcid.org/0000-0002-5572-508X; Phone: 86-24-31329999; Email: hcsun@jlu.edu.cn; Fax: 86-24-31927811

Authors

Wenhuan Bu − *Liaoning Provincial Key Laboratory of Oral Diseases, School of Stomatology, Department of Dental Materials, School of Stomatology, Department of Oral Pathology, School of Stomatology, and Department of Center Laboratory, School of Stomatology, China Medical University, Shenyang 110001, China*

Xiaowei Xu − *Department of Periodontology, School and Hospital of Stomatology, Jilin University, Changchun 130021, China*; orcid.org/0000-0003-4863-112X

Zilin Wang − *Department of Oral Pathology, School and Hospital of Stomatology, Jilin University, Changchun 130021, China*

Nianqiang Jin − *Liaoning Provincial Key Laboratory of Oral Diseases, School of Stomatology, China Medical University, Shenyang 110001, China*

https://dx.doi.org/10.1021/acsami.0c15425
ACS Appl. Mater. Interfaces 2020, 12, 50287−50302

Lili Liu − *Department of Oral Pathology, School and Hospital of Stomatology, Jilin University, Changchun 130021, China*
Jie Liu − *Department of Oral and Maxillofacial Surgery, School of Stomatology, Wuhan University, Wuhan 430000, China*
Shoujun Zhu − *State Key Laboratory of Supramolecular Structure and Materials, College of Chemistry, Jilin University, Changchun 130012, China;* orcid.org/0000-0002-2412-6121
Kai Zhang − *State Key Laboratory of Supramolecular Structure and Materials, College of Chemistry, Jilin University, Changchun 130012, China;* orcid.org/0000-0002-5507-3528
Raz Jelinek − *Department of Chemistry, Ilse Katz Institute for Nanotechnology, Ben Gurion University of the Negev, Beer Sheva 8410501, Israel;* orcid.org/0000-0002-0336-1384
Bai Yang − *State Key Laboratory of Supramolecular Structure and Materials, College of Chemistry, Jilin University, Changchun 130012, China;* orcid.org/0000-0002-3873-075X

Complete contact information is available at: https://pubs.acs.org/10.1021/acsami.0c15425

Author Contributions

The manuscript was written through contributions of all authors. All authors have given approval to the final version of the manuscript.

Notes

The authors declare no competing financial interest.

■ ACKNOWLEDGMENTS

We thank Dr. Yuji Mishina from the University of Michigan for his technical support and Dr. Jian Xu from the University of Southern California for her critical reading. This study was supported by grants from the National Key R&D Program of China (2016YFC1102800 to H.S.), the National Natural Science Foundation of China (81870741 to H.S., 82001023 to W.B., 81920108012 to H.S., 81320108011 to H.S.), China Postdoctoral Science Foundation (2019M661177 to W.B.), State Key Laboratory of Luminescence and Applications (SKLA-2020-07 to H.S.), Jilin Scientific and Technological Development Program (20170101093JC to W.B.), Provincial Industrial Innovation Project of Jilin Province (2016C044-3 to W.B.), and Natural Science Foundation of Liaoning Province (2020-MS-154 to W.B.).

■ REFERENCES

(1) Cao, X.; Wu, X.; Frassica, D.; Yu, B.; Pang, L.; Xian, L.; Wan, M.; Lei, W.; Armour, M.; Tryggestad, E.; Wong, J.; Wen, C. Y.; Lu, W. W.; Frassica, F. J. Irradiation Induces Bone Injury by Damaging Bone Marrow Microenvironment for Stem Cells. *Proc. Natl. Acad. Sci. U. S. A.* **2011**, *108*, 1609−1614.
(2) Dimitriou, R.; Jones, E.; McGonagle, D.; Giannoudis, P. V. Bone Regeneration: Current Concepts and Future Directions. *BMC Med.* **2011**, *9*, 66.
(3) Ivey, K. N.; Srivastava, D. Micrornas as Regulators of Differentiation and Cell Fate Decisions. *Cell Stem Cell* **2010**, *7*, 36−41.
(4) Muthiah, M.; Park, I. K.; Cho, C. S. Nanoparticle-Mediated Delivery of Therapeutic Genes: Focus on MiRNA Therapeutics. *Expert Opin. Drug Delivery* **2013**, *10*, 1259−1273.
(5) Lacoste, A.; Berenshteyn, F.; Brivanlou, A. H. An Efficient and Reversible Transposable System for Gene Delivery and Lineage-Specific Differentiation in Human Embryonic Stem Cells. *Cell Stem Cell* **2009**, *5*, 332−342.
(6) Zhang, J. F.; Fu, W. M.; He, M. L.; Xie, W. D.; Lv, Q.; Wan, G.; Li, G.; Wang, H.; Lu, G.; Hu, X.; Jiang, S.; Li, J. N.; Lin, M. C.; Zhang, Y. O.; Kung, H. F. Mirna-20a Promotes Osteogenic Differentiation of Human Mesenchymal Stem Cells by Co-Regulating Bmp Signaling. *RNA Biol.* **2011**, *8*, 829−838.
(7) Li, Z.; Hassan, M. Q.; Jafferji, M.; Aqeilan, R. I.; Garzon, R.; Croce, C. M.; van Wijnen, A. J.; Stein, J. L.; Stein, G. S.; Lian, J. B. Biological Functions of Mir-29b Contribute to Positive Regulation of Osteoblast Differentiation. *J. Biol. Chem.* **2009**, *284*, 15676−15684.
(8) Luzi, E.; Marini, F.; Sala, S. C.; Tognarini, I.; Galli, G.; Brandi, M. L. Osteogenic Differentiation of Human Adipose Tissue-Derived Stem Cells Is Modulated by the Mir-26a Targeting of the Smad1 Transcription Factor. *J. Bone Miner. Res.* **2008**, *23*, 287−295.
(9) Eskildsen, T.; Taipaleenmaki, H.; Stenvang, J.; Abdallah, B. M.; Ditzel, N.; Nossent, A. Y.; Bak, M.; Kauppinen, S.; Kassem, M. MicroRNA-138 Regulates Osteogenic Differentiation of Human Stromal (Mesenchymal) Stem Cells *in Vivo*. *Proc. Natl. Acad. Sci. U. S. A.* **2011**, *108*, 6139−6144.
(10) Li, H.; Xie, H.; Liu, W.; Hu, R.; Huang, B.; Tan, Y. F.; Xu, K.; Sheng, Z. F.; Zhou, H. D.; Wu, X. P.; Luo, X. H. A Novel MicroRNA Targeting HDAC5 Regulates Osteoblast Differentiation in Mice and Contributes to Primary Osteoporosis in Humans. *J. Clin. Invest.* **2009**, *119*, 3666−3677.
(11) Hu, R.; Liu, W.; Li, H.; Yang, L.; Chen, C.; Xia, Z. Y.; Guo, L. J.; Xie, H.; Zhou, H. D.; Wu, X. P.; Luo, X. H. A Runx2/miR-3960/miR-2861 Regulatory Feedback Loop during Mouse Osteoblast Differentiation. *J. Biolog. Chem.* **2011**, *286*, 12328−12339.
(12) Yau, W. W. Y.; Rujitanaroj, P. O.; Lam, L.; Chew, S. Y. Directing Stem Cell Fate by Controlled RNA Interference. *Biomaterials* **2012**, *33*, 2608−2628.
(13) Mintzer, M. A.; Simanek, E. E. Nonviral Vectors for Gene Delivery. *Chem. Rev.* **2008**, *109*, 259−302.
(14) Crew, E.; Rahman, S.; Razzak-Jaffar, A.; Mott, D.; Kamundi, M.; Yu, G.; Tchah, N.; Lee, J.; Bellavia, M.; Zhong, C. J. MicroRNA Conjugated Gold Nanoparticles and Cell Transfection. *Anal. Chem.* **2012**, *84*, 26−29.
(15) Schade, A.; Delyagina, E.; Scharfenberg, D.; Skorska, A.; Lux, C.; David, R.; Steinhoff, G. Innovative Strategy for MicroRNA Delivery in Human Mesenchymal Stem Cells via Magnetic Nanoparticles. *Int. J. Mol. Sci.* **2013**, *14*, 10710−10726.
(16) Bitar, A.; Ahmad, N. M.; Fessi, H.; Elaissari, A. Silica-Based Nanoparticles for Biomedical Applications. *Drug Discovery Today* **2012**, *17*, 1147−1154.
(17) Kou, L.; Sun, J.; Zhai, Y.; He, Z. The Endocytosis and Intracellular Fate of Nanomedicines: Implication for Rational Design. *Asian J. Pharm. Sci.* **2013**, *8*, 1−10.
(18) Zhu, S.; Wang, L.; Zhou, N.; Zhao, X.; Song, Y.; Maharjan, S.; Zhang, J.; Lu, L.; Wang, H.; Yang, B. The Crosslink Enhanced Emission (Cee) in Non-Conjugated Polymer Dots: From the Photoluminescence Mechanism to the Cellular Uptake Mechanism and Internalization. *Chem. Commun.* **2014**, *50*, 13845−13848.
(19) Mao, S.; Neu, M.; Germershaus, O.; Merkel, O.; Sitterberg, J.; Bakowsky, U.; Kissel, T. Influence of Polyethylene Glycol Chain Length on the Physicochemical and Biological Properties of Poly(ethylene imine)-*graft*-Poly(ethylene glycol) Block Copolymer/SiRNA Polyplexes. *Bioconjugate Chem.* **2006**, *17*, 1209−1218.
(20) Xu, X.; Ray, R.; Gu, Y.; Ploehn, H. J.; Gearheart, L.; Raker, K.; Scrivens, W. A. Electrophoretic Analysis and Purification of Fluorescent Single-Walled Carbon Nanotube Fragments. *J. Am. Chem. Soc.* **2004**, *126*, 12736−12737.
(21) Lim, S. Y.; Shen, W.; Gao, Z. Carbon Quantum Dots and Their Applications. *Chem. Soc. Rev.* **2015**, *44*, 362−381.
(22) Peng, H.; Travas-Sejdic, J. Simple Aqueous Solution Route to Luminescent Carbogenic Dots from Carbohydrates. *Chem. Mater.* **2009**, *21*, 5563−5565.
(23) Zhang, Y.-Q.; Ma, D.-K.; Zhuang, Y.; Zhang, X.; Chen, W.; Hong, L.-L.; Yan, Q.-X.; Yu, K.; Huang, S.-M. One-Pot Synthesis of N-Doped Carbon Dots with Tunable Luminescence Properties. *J. Mater. Chem.* **2012**, *22*, 16714−16718.

(24) Wang, W.; Li, Y.; Cheng, L.; Cao, Z.; Liu, W. Water-Soluble and Phosphorus-Containing Carbon Dots with Strong Green Fluorescence for Cell Labeling. *J. Mater. Chem. B* **2013**, *2*, 46−48.
(25) Ding, C.; Zhu, A.; Tian, Y. Functional Surface Engineering of C-Dots for Fluorescent Biosensing and *in Vivo* Bioimaging. *Acc. Chem. Res.* **2014**, *47*, 20−30.
(26) Zhu, S.; Song, Y.; Zhao, X.; Shao, J.; Zhang, J.; Yang, B. The Photoluminescence Mechanism in Carbon Dots (Graphene Quantum Dots, Carbon Nanodots, and Polymer Dots): Current State and Future Perspective. *Nano Res.* **2015**, *8*, 355−381.
(27) Feng, T.; Ai, X.; An, G.; Yang, P.; Zhao, Y. Charge-Convertible Carbon Dots for Imaging-Guided Drug Delivery with Enhanced *in Vivo* Cancer Therapeutic Efficiency. *ACS Nano* **2016**, *10*, 4410−4420.
(28) Wang, Z.; Yuan, F.; Li, X.; Li, Y.; Zhong, H.; Fan, L.; Yang, S. 53% Efficient Red Emissive Carbon Quantum Dots for High Color Rendering and Stable Warm White-Light-Emitting Diodes. *Adv. Mater.* **2017**, *29*, 1792910.
(29) Yu, H.; Shi, R.; Zhao, Y.; Waterhouse, G. I.; Wu, L. Z.; Tung, C. H.; Zhang, T. Smart Utilization of Carbon Dots in Semiconductor Photocatalysis. *Adv. Mater.* **2016**, *28*, 9454−9477.
(30) Du, F.; Zhang, L.; Zhang, L.; Zhang, M.; Gong, A.; Tan, Y.; Miao, J.; Gong, Y.; Sun, M.; Ju, H.; Wu, C.; Zou, S. Engineered Gadolinium-Doped Carbon Dots for Magnetic Resonance Imaging-Guided Radiotherapy of Tumors. *Biomaterials* **2017**, *121*, 109−120.
(31) Kim, D.; Yoo, J. M.; Hwang, H.; Lee, J.; Lee, S. H.; Yun, S. P.; Park, M. J.; Lee, M.; Choi, S.; Kwon, S. H.; Lee, S. Graphene Quantum Dots Prevent α-Synucleinopathy in Parkinson's Disease. *Nat. Nanotechnol.* **2018**, *13*, 812−818.
(32) Jia, Q.; Ge, J.; Liu, W.; Zheng, X.; Chen, S.; Wen, Y.; Zhang, H.; Wang, P. A Magnetofluorescent Carbon Dot Assembly as an Acidic H_2O_2-Driven Oxygenerator to Regulate Tumor Hypoxia for Simultaneous Bimodal Imaging and Enhanced Photodynamic Therapy. *Adv. Mater.* **2018**, *30*, 1706090.
(33) Shao, D.; Lu, M.; Xu, D.; Zheng, X.; Pan, Y.; Song, Y.; Xu, J.; Li, M.; Zhang, M.; Li, J.; Chi, G.; Chen, L.; Yang, B. Carbon Dots for Tracking and Promoting the Osteogenic Differentiation of Mesenchymal Stem Cells. *Biomater. Sci.* **2017**, *5*, 1820−1827.
(34) Yang, M.; Meng, Y.; Liu, J.; Yu, W.; Yang, B. Facile Synthesis of Mg^{2+}-Doped Carbon Dots as Novel Biomaterial Inducing Cell Osteoblastic Differentiation. *Part. Part. Syst. Charact.* **2019**, *36*, 1800315.
(35) Khajuria, D. K.; Kumar, V. B.; Gigi, D.; Gedanken, A.; Karasik, D. Accelerated Bone Regeneration by Nitrogen-Doped Carbon Dots Functionalized with Hydroxyapatite Nanoparticles. *ACS Appl. Mater. Interfaces* **2018**, *10*, 19373−19385.
(36) Zhao, F.; Zhao, Y.; Liu, Y.; Chang, X.; Chen, C.; Zhao, Y. Cellular Uptake, Intracellular Trafficking, and Cytotoxicity of Nanomaterials. *Small* **2011**, *7*, 1322−1337.
(37) Rappoport, J. Z. Focusing on Clathrin-Mediated Endocytosis. *Biochem. J.* **2008**, *412*, 415−423.
(38) Gong, J.; An, X.; Yan, X. A Novel Rapid and Green Synthesis of Highly Luminescent Carbon Dots with Good Biocompatibility for Cell Imaging. *New J. Chem.* **2014**, *38*, 1376−1379.
(39) Fu, M.; Ehrat, F.; Wang, Y.; Milowska, K. Z.; Reckmeier, C.; Rogach, A. L.; Stolarczyk, J. K.; Urban, A. S.; Feldmann, J. Carbon Dots: A Unique Fluorescent Cocktail of Polycyclic Aromatic Hydrocarbons. *Nano Lett.* **2015**, *15*, 6030−6035.
(40) Zhang, B.; Liu, C. Y.; Liu, Y. A Novel One-Step Approach to Synthesize Fluorescent Carbon Nanoparticles. *Eur. J. Inorg. Chem.* **2010**, *2010*, 4411−4414.
(41) Bao, L.; Zhang, Z. L.; Tian, Z. Q.; Zhang, L.; Liu, C.; Lin, Y.; Qi, B.; Pang, D. W. Electrochemical Tuning of Luminescent Carbon Nanodots: From Preparation to Luminescence Mechanism. *Adv. Mater.* **2011**, *23*, 5801−5806.
(42) Tang, L.; Ji, R.; Cao, X.; Lin, J.; Jiang, H.; Li, X.; Teng, K. S.; Luk, C. M.; Zeng, S.; Hao, J.; Lau, S. P. Deep Ultraviolet Photoluminescence of Water-Soluble Self-Passivated Graphene Quantum Dots. *ACS Nano* **2012**, *6*, 5102−5110.
(43) Mosesson, Y.; Mills, G. B.; Yarden, Y. Derailed Endocytosis: An Emerging Feature of Cancer. *Nat. Rev. Cancer* **2008**, *8*, 835−850.
(44) Almeida, J. P. M.; Chen, A. L.; Foster, A.; Drezek, R. In Vivo Biodistribution of Nanoparticles. *Nanomedicine* **2011**, *6*, 815−835.
(45) Longmire, M.; Choyke, P. L.; Kobayashi, H. Clearance Properties of Nano-Sized Particles and Molecules as Imaging Agents: Considerations and Caveats. *Nanomedicine* **2008**, *3*, 703−717.
(46) Papisov, M. I.; Bogdanov, A.; Schaffer, B.; Nossiff, N.; Shen, T.; Weissleder, R.; Brady, T. J. Colloidal Magnetic-Resonance Contrast Agents: Effect of Particle Surface on Biodistribution. *J. Magn. Magn. Mater.* **1993**, *122*, 383−386.
(47) Huang, X.; Li, L.; Liu, T.; Hao, N.; Liu, H.; Chen, D.; Tang, F. The Shape Effect of Mesoporous Silica Nanoparticles on Biodistribution, Clearance, and Biocompatibility in Vivo. *ACS Nano* **2011**, *5*, 5390−5399.
(48) Liu, P.; Sun, Y.; Wang, Q.; Sun, Y.; Li, H.; Duan, Y. Intracellular Trafficking and Cellular Uptake Mechanism of mPEG-PLGA-PLL and mPEG-PLGA-PLL-Gal Nanoparticles for Targeted Delivery to Hepatomas. *Biomaterials* **2014**, *35*, 760−770.
(49) Cheng, G.; Li, W.; Ha, L.; Han, X.; Hao, S.; Wan, Y.; Wang, Z.; Dong, F.; Zou, X.; Mao, Y.; Zheng, S. Y. Self-Assembly of Extracellular Vesicle-Like Metal-Organic Framework Nanoparticles for Protection and Intracellular Delivery of Biofunctional Proteins. *J. Am. Chem. Soc.* **2018**, *140*, 7282−7291.
(50) Los, D. A.; Murata, N. Membrane Fluidity and Its Roles in the Perception of Environmental Signals. *Biochim. Biophys. Acta* **2004**, *1666*, 142−157.
(51) Gutu, M.; Rusu, V.; Stefanescu, C. Membrane Fluidity–Biophysical Parameter in Relation to Membrane Transport Processes. *Rev. Med. Chir. Soc. Med. Nat. Iasi* **2011**, *115*, 153−162.
(52) Zhou, N.; Zhu, S.; Maharjan, S.; Hao, Z.; Song, Y.; Zhao, X.; Jiang, Y.; Yang, B.; Lu, L. Elucidating the Endocytosis, Intracellular Trafficking, and Exocytosis of Carbon Dots in Neural Cells. *RSC Adv.* **2014**, *4*, 62086−62095.
(53) Canton, I.; Battaglia, G. Endocytosis at the Nanoscale. *Chem. Soc. Rev.* **2012**, *41*, 2718−2739.
(54) Wu, C.; Wang, C.; Han, T.; Zhou, X.; Guo, S.; Zhang, J. Insight into the Cellular Internalization and Cytotoxicity of Graphene Quantum Dots. *Adv. Healthcare Mater.* **2013**, *2*, 1613−1619.
(55) Petros, R. A.; DeSimone, J. M. Strategies in the Design of Nanoparticles for Therapeutic Applications. *Nat. Rev. Drug Discovery* **2010**, *9*, 615−627.
(56) Franceschi, R. T.; Iyer, B. S.; Cui, Y. Effects of Ascorbic Acid on Collagen Matrix Formation and Osteoblast Differentiation in Murine MC3T3-E1 Cells. *J. Bone Miner. Res.* **1994**, *9*, 843−854.
(57) Golub, E. E.; Boesze-Battaglia, K. The Role of Alkaline Phosphatase in Mineralization. *Curr. Opin. Orthop.* **2007**, *18*, 444−448.
(58) Blair, H. C.; Larrouture, Q. C.; Li, Y.; Lin, H.; Beer-Stoltz, D.; Liu, L.; Tuan, R. S.; Robinson, L. J.; Schlesinger, P. H.; Nelson, D. J. Osteoblast Differentiation and Bone Matrix Formation *in Vivo* and *in Vitro*. *Tissue Eng., Part B* **2017**, *23*, 268−280.
(59) Ducy, P.; Zhang, R.; Geoffroy, V.; Ridall, A. L.; Karsenty, G. Osf2/Cbfa1: A Transcriptional Activator of Osteoblast Differentiation. *Cell* **1997**, *89*, 747−754.
(60) Nakashima, K.; Zhou, X.; Kunkel, G.; Zhang, Z.; Deng, J. M.; Behringer, R. R.; De Crombrugghe, B. The Novel Zinc Finger-Containing Transcription Factor Osterix Is Required for Osteoblast Differentiation and Bone Formation. *Cell* **2002**, *108*, 17−29.
(61) Nishio, Y.; Dong, Y.; Paris, M.; O'Keefe, R. J.; Schwarz, E. M.; Drissi, H. Runx2-Mediated Regulation of the Zinc Finger Osterix/Sp7 Gene. *Gene* **2006**, *372*, 62−70.
(62) Sayed, N.; Tambe, P.; Kumar, P.; Jadhav, S.; Paknikar, K. M.; Gajbhiye, V. MiRNA Transfection via Poly (amidoamine)-Based Delivery Vector Prevents Hypoxia/Reperfusion-Induced Cardiomyocyte Apoptosis. *Nanomedicine* **2020**, *15*, 163−181.
(63) Kapadia, C. H.; Luo, B.; Dang, M. N.; Irvin-Choy, N. D.; Valcourt, D. M.; Day, E. S. Polymer Nanocarriers for MicroRNA Delivery. *J. Appl. Polym. Sci.* **2020**, *137*, 48651.

https://dx.doi.org/10.1021/acsami.0c15425
ACS Appl. Mater. Interfaces 2020, 12, 50287−50302

(64) Pizzicannella, J.; Diomede, F.; Gugliandolo, A.; Chiricosta, L.; Bramanti, P.; Merciaro, I.; Orsini, T.; Mazzon, E.; Trubiani, O. 3D Printing PLA/Gingival Stem Cells/EVs Upregulate MiR-2861 and-210 during Osteoangiogenesis Commitment. *Int. J. Mol. Sci.* **2019**, *20*, 3256.
(65) Sun, Y.; Ye, X.; Cai, M.; Liu, X.; Xiao, J.; Zhang, C.; Wang, Y.; Yang, L.; Liu, J.; Li, S.; Kang, C.; Zhang, B.; Zhang, Q.; Wang, Z.; Hong, A.; Wang, X. Osteoblast-Targeting-Peptide Modified Nanoparticle for SiRNA/MicroRNA Delivery. *ACS Nano* **2016**, *10*, 5759−5768.
(66) Lei, L.; Liu, Z.; Yuan, P.; Jin, R.; Wang, X.; Jiang, T.; Chen, X. Injectable Colloidal Hydrogel with Mesoporous Silica Nanoparticles for Sustained Co-Release of MicroRNA-222 and Aspirin to Achieve Innervated Bone Regeneration in Rat Mandibular Defects. *J. Mater. Chem. B* **2019**, *7*, 2722−2735.
(67) Sui, L.; Wang, M.; Han, Q.; Yu, L.; Zhang, L.; Zheng, L.; Lian, J.; Zhang, J.; Valverde, P.; Xu, Q.; Tu, Q.; Chen, J. A Novel Lipidoid-MicroRNA Formulation Promotes Calvarial Bone Regeneration. *Biomaterials* **2018**, *177*, 88−97.
(68) Wu, G.; Feng, C.; Quan, J.; Wang, Z.; Wei, W.; Zang, S.; Kang, S.; Hui, G.; Chen, X.; Wang, Q. *In Situ* Controlled Release of Stromal Cell-Derived Factor-1α and AntimiR-138 for on-Demand Cranial Bone Regeneration. *Carbohydr. Polym.* **2018**, *182*, 215−224.
(69) Wang, P.; Liu, X.; Zhao, L.; Weir, M. D.; Sun, J.; Chen, W.; Man, Y.; Xu, H. H. K. Bone Tissue Engineering via Human Induced Pluripotent, Umbilical Cord and Bone Marrow Mesenchymal Stem Cells in Rat Cranium. *Acta Biomater.* **2015**, *18*, 236−248.
(70) Yao, Q.; Cosme, J. G. L.; Xu, T.; Miszuk, J. M.; Picciani, P. H. S.; Fong, H.; Sun, H. Three Dimensional Electrospun PCL/PLA Blend Nanofibrous Scaffolds with Significantly Improved Stem Cells Osteogenic Differentiation and Cranial Bone Formation. *Biomaterials* **2017**, *115*, 115−127.

https://dx.doi.org/10.1021/acsami.0c15425
ACS Appl. Mater. Interfaces 2020, 12, 50287−50302